

Chapter 8

Plasmonic Gas and Chemical Sensing

Andreas Tittl, Harald Giessen, and Na Liu

Abstract Sensitive and robust detection of gases and chemical reactions constitutes a cornerstone of scientific research and industrial applications. In an effort to reach progressively smaller reagent concentrations and sensing volumes, optical sensor technology has experienced a paradigm shift from extended thin-film systems towards engineered nanoscale devices. In this size regime, plasmonic particles and nanostructures provide an ideal toolkit for the realization of novel sensing concepts. This is due to their unique ability to simultaneously focus light into subwavelength hotspots of the electromagnetic field and to transmit minute changes of the local environment back into the farfield as a modulation of their optical response. Since the basic building blocks of a plasmonic system are commonly noble metal nanoparticles or nanostructures, plasmonics can easily be integrated with a plethora of chemically or catalytically active materials and compounds to detect processes ranging from hydrogen absorption in palladium to the detection of trinitrotoluene (TNT). In this review, we will discuss a multitude of plasmonic sensing strategies, spanning the technological scale from simple plasmonic particles embedded in extended films to highly engineered complex plasmonic nanostructures. Due to their flexibility and excellent sensing performance, plasmonic structures may open an exciting pathway towards the detection of chemical and catalytic events down to the single molecule level.

A. Tittl • H. Giessen
4th Physics Institute and Research Center Scope, University of Stuttgart, D-70569 Stuttgart,
Germany
e-mail: h.giessen@pi4.uni-stuttgart.de

N. Liu (✉)
Max Planck Institute for Intelligent Systems, Heisenbergstrasse 3, D-70569 Stuttgart, Germany
e-mail: laura.liu@is.mpg.de

8.1 Introduction

In the last decade, plasmonics has developed into an expansive and vibrant field, with applications as diverse as negative refraction, enhanced photovoltaics, and targeted drug delivery [1–3]. This progress has been driven by major advances in the fabrication of nanostructured systems, including both “top-down” approaches such as electron-beam or nanoimprint lithography as well as “bottom-up” techniques like nanosphere lithography [4–6]. The unprecedented ability to structure metals and dielectrics on the nanoscale has allowed plasmonics to move from giga- and terahertz into the near-infrared and visible spectral ranges. Since the response of plasmonic structures in the latter range allows for remote and non-invasive read-out using standard optical spectroscopy, this move has been a crucial driving factor for the field of plasmonic sensing [7–11].

Most plasmonic sensing concepts rely on the ability of small metal particles to concentrate incident light into deep subwavelength volumes. This behavior is due to the collective oscillations of the conduction electrons against the restoring force of the positively charged nuclei, which can be resonantly driven by an external electromagnetic field [12]. The spectral behavior of such plasmonic resonances can be calculated analytically for geometrically simple systems, such as a subwavelength gold sphere in vacuum, yielding a Lorentzian lineshape. However, for more complex systems, the plasmon resonance position and lineshape are highly dependent on the composition, geometry, and dielectric environment of the nanostructure [13].

The greatly enhanced electromagnetic fields at the surface of a resonant plasmonic structure allow it to probe minute changes in the surrounding environment. Due to the evanescent nature of the fields, the sensing volume of plasmonic nanostructures is only marginally larger than the structures themselves, making them ideal local probes for neighboring changes in a medium. Consequently, plasmonic probes are especially relevant for monitoring of chemical or catalytic reactions, where the reaction efficiency can crucially depend on localized changes in reagent concentration or catalyst morphology.

In order to quantify the sensing performance of a plasmonic system, we can consider its refractive index sensitivity S , defined as the peak shift in nanometers of the plasmonic resonance per refractive index unit (RIU). However, since the final accuracy of the peak tracking depends both on the magnitude of the peak shift and on the resonance linewidth, a more suitable choice for plasmonic systems is the figure of merit (FOM), namely, dividing the refractive index sensitivity by the resonance linewidth.

Thus there are two key approaches for optimizing the figure of merit in a plasmonic sensing geometry: reducing the resonance linewidth, and increasing the peak shift by boosting the local field-enhancement. In general, plasmon oscillations in nanoparticles experience damping arising from two contributions: intrinsic damping due electron-electron collisions and impurity scattering in the metal, and radiation damping due to the direct decay of the collective oscillations into photons. Utilizing noble metals for the resonant nanoparticles helps to reduce

intrinsic damping. However, radiation damping, which constitutes the dominating effect for particles larger than a few tens of nanometers, cannot easily be overcome in simple plasmonic systems [14, 15].

By arranging multiple plasmonic particles into a defined geometry, coupling effects may happen and can significantly reduce the linewidth of the plasmonic resonance [16]. One way to achieve this is to couple a broad dipolar plasmonic resonance to a spectrally narrow quadrupolar mode, which cannot be excited from the farfield. The coupling of two such modes can lead to a narrow spectral feature in the otherwise broad dipolar lineshape, which exhibits a greatly increased FOM compared to simple plasmonic structures in the same spectral range, a feature known as the plasmonic analogue of electromagnetically induced transparency (EIT) [17–19].

In order to increase the electromagnetic field-enhancement, plasmonics has taken cues from classical antenna theory. In triangular “bowtie” nanoparticle geometries, the electromagnetic fields can be enhanced and concentrated at the tips of the structure. By utilizing complex Yagi-Uda antenna designs to the nanoscale, efficient and directed energy transfer between the far-field and the near-field can be realized [20, 21]. Using the coupling between, e.g., two rod-type nanoantennas can further enhance the near-fields compared to single antenna elements. When decreasing the distance between the two rods, the electromagnetic fields can be confined to a progressively smaller volume, leading to extremely high enhancement factors, only limited by fabrication tolerances and quantum mechanical tunneling effects below sub 1 nm gaps [22–24].

When such highly sensitive plasmonic structures are adapted for sensing applications, two main concepts for the detection of gases and chemical reagents emerge: in *direct* sensing configurations, the reagents actively influence the plasmonic entity, changing its material properties and in turn its optical response, whereas in *indirect* sensing schemes, the plasmonic structure is located adjacent to some reagent-sensitive material and simply probes the dielectric changes in that system [25].

One experimental issue connecting both sensing schemes is the correlation of gas or reagent concentration changes with changes in the optical response. To facilitate this analysis, one commonly extracts a single “sensor signal” value from the full spectral response. Depending on the system under consideration, observables such as the intensity at a given wavelength, the resonance position, or the resonance peak’s full width at half maximum (FWHM) can be tracked in relation to environmental changes. This allows for a straightforward characterization and performance comparison between plasmonic sensor designs with different structural and configurational parameters.

In the following, we will review both direct and indirect sensing schemes, covering a wide technological range from plasmonically functionalized thin films through highly engineered chemically grown particles composed of multiple materials all the way up to complex nanostructured geometries. The presented sensor devices are selected to showcase the wide array of reagents that can be investigated using plasmonic systems as well as the most versatile and high-performance complex plasmonic nanoprobcs. By combining such highly sensitive nanodevices with novel

reagent-specific materials, plasmonic sensors can be used to investigate a plethora of chemically and biologically significant reagents, with nanometer spatial resolution and possible down to the single molecule level.

8.2 Thin Films with Embedded Plasmonic Particles

One straightforward approach to optical sensing is the use of thin films of reagent-sensitive material deposited on a substrate. Such films combine robust fabrication via standard evaporation or sputtering techniques with simple optical transmission or reflection measurements for read-out [26, 27].

In order to enhance the sensor performance and tailor the optical response of such thin films, small plasmonic particles can be added using co-deposition or multi-step processes. When considering thin films with embedded plasmonic particles, two main concepts can be distinguished. In *plasmonically enhanced* systems, small noble metal particles in the thin film act simply as light concentrators and probes to enhance the dielectric changes in the surrounding material. In *catalytically enhanced* systems, gold nanoparticles in direct contact with, e.g., transition metal oxide films can substantially increase the catalytic activity of such material systems. Here, the optical response stems largely from changes in the transition metal oxide. In the following, we will first focus on two examples of catalytically enhanced thin-film systems.

8.2.1 Carbon Monoxide Sensing with Plasmonically Functionalized Thin Films

Due to its high toxicity, sensitive and reliable detection of carbon monoxide is vital for industrial process and environmental monitoring applications. Ando et al. have demonstrated a plasmonically functionalized Au-CuO nanocomposite film for CO sensing, fabricated by first depositing Au particles on a substrate via DC sputtering and then covering them with a CuO film via pyrolysis [28]. Figure 8.1a shows a transmission electron microscope (TEM) image of the nanocomposite film, where small Au particles of average diameter 24 nm surrounded by a CuO matrix can be clearly identified. The authors performed absorbance measurements at a temperature of 300 °C and observed a plasmonic absorbance peak at a wavelength of around 800 nm. The magnitude of this peak increased substantially upon exposure of the film to 1,000 ppm and 1 % CO in dry air (Fig. 8.1b). In addition, when calibrating their sensor device with various concentrations of CO in dry air, the authors found a linear relation between the absorbance change and the logarithm of the CO concentration over a wide range from 50 to 10,000 ppm CO in dry air (Fig. 8.1c), allowing for straightforward quantitative sensing.

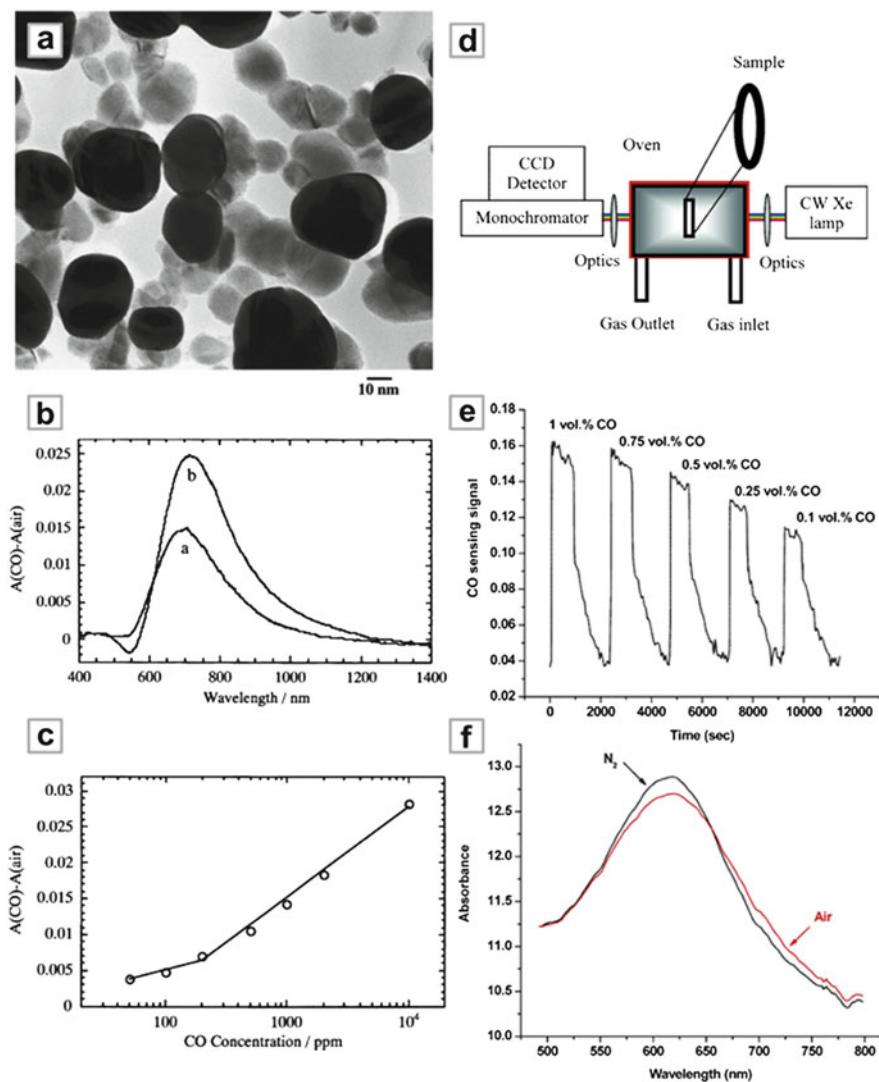


Fig. 8.1 Carbon monoxide sensing with plasmonically functionalized thin films. (a) Transmission electron microscope image of a Au-CuO nanocomposite film. (b) Relative CO-induced absorbance change of the Au-CuO composite film. (c) Correlation between CO concentration and relative absorbance change (a–c from [28]). (d) Schematic of a setup used for high temperature CO sensing experiments. (e) Sensing signal response curve of the Au-YSZ nanocomposite film at 500 °C. (f) Absorbance of the Au-YSZ nanocomposite film in N_2 and air atmosphere at 500 °C (d–f from [29])

A similar approach for the detection of CO was presented by Sirinakis et al. who used gold nanoparticles embedded in an yttria-stabilized zirconia (YSZ) matrix [29]. Their device was fabricated using radio frequency magnetron co-sputtering followed by an annealing process and optical characterization was performed in

a quartz transmission cell surrounded by a tube furnace (Fig. 8.1d). The authors observed a pronounced Lorentz-like absorbance peak at a wavelength of around 600 nm, which spectrally narrowed and blueshifted upon CO exposure. This change allowed the authors to detect CO concentrations ranging from 0.1 to 1 vol.% in dry air at a temperature of 500 °C (Fig. 8.1e). However, they observed no change in the optical response when exposing their sample to CO in nitrogen carrier gas. The authors attributed this behavior to the reactivity of the YSZ film to oxygen, since switching from nitrogen carrier gas to dry air already introduced a broadening and redshift of the plasmon resonance in their system (Fig. 8.1f). This allowed them to explain the blueshift and narrowing of the plasmon resonance through charge transfer into the Au nanoparticles caused by the oxidation of CO and the corresponding reduction of the YSZ matrix at high temperatures. This behavior makes the system by Sirinakis et al. a prime example of *catalytically enhanced* sensing with plasmonically functionalized thin films.

8.2.2 Hydrogen Sensing with Plasmonically Functionalized Thin Films

Other than carbon monoxide, hydrogen detection is an additional safety factor in large-scale industrial chemical processing [30]. Hydrogen forms a combustible mixture with air at concentrations ranging from 4 to 76 vol.%, which can be ignited easily with sparks or at a sufficiently high temperature. Therefore, sensitive hydrogen detection is a cornerstone of alternative energy concepts such as water splitting or, in more general terms, solar-to-chemical energy conversion [31].

In this framework, Buso et al. have utilized a SiO₂ matrix containing Au and NiO nanoparticles for sensitive detection of hydrogen, where the SiO₂ matrix was chosen due to its extremely high specific surface area [32]. High-resolution TEM images in Fig. 8.2a show the evenly distributed Au particles embedded in the SiO₂ host material, surrounded by finely dispersed crystallite NiO particles. In optical measurements, the authors found a plasmon resonance peak at a wavelength of 563 nm, which underwent a drastic blueshift of 22 nm when exposing the sensor device to 1 vol.% H₂ in dry air. This pronounced change in the optical behavior (Fig. 8.2b) could not be sufficiently explained in terms of catalytic charge transfer into the Au particle, which led the authors to relate their system to *plasmonically enhanced* detection of hydrogen. There was, however, a second sensing pathway when exposing the sensor device to CO with a weaker but still measurable response (Fig. 8.2b). The authors assumed an injection of electrons from the NiO crystallites into the Au nanoparticles during CO exposure and subsequent oxidation, which led to the observed changes in the plasmonic response. Thus, their system combined both plasmonically and catalytically enhanced approaches for detection of hydrogen and carbon monoxide.

In a further study on this system, Dharmalingam et al. investigated Au-YSZ nanocomposite films for varying sizes of the embedded Au particles for detection

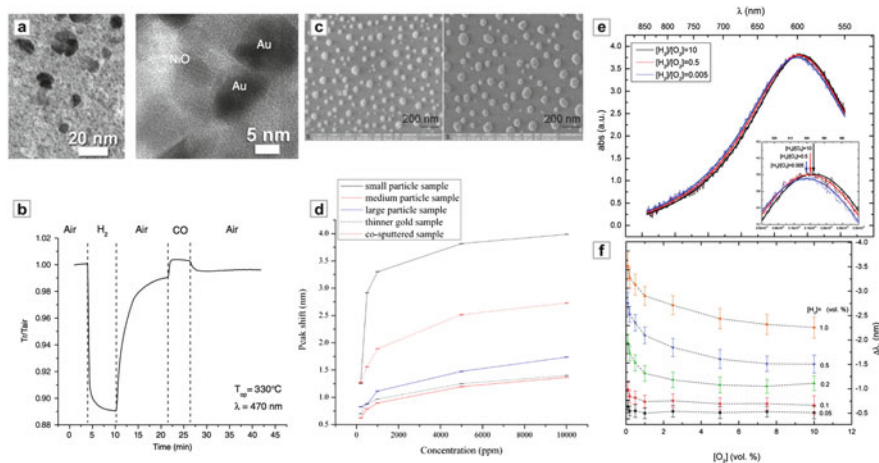


Fig. 8.2 Hydrogen sensing with plasmonically functionalized thin films. **(a)** Cross-sectional and high-resolution TEM images of a SiO₂ matrix containing Au and NiO nanoparticles. **(b)** Dynamic optical response of a film containing 6 % Au exposed to cycles of 1 vol.% H₂ in air and 1 vol.% CO in air (**a, b** from [32]). **(c)** SEM images of small-particle and medium-particle Au-YSZ nanocomposite films. **(d)** Hydrogen sensing calibration curves for nanocomposite samples with different particle sizes and preparation methods (**c, d** from [33]). **(e)** Absorbance spectra and Lorentzian fits for a Au-YSZ film under various redox conditions at 500 °C. **(f)** Change in plasmon resonance position as a function of O₂ concentration upon exposure to various concentrations of H₂ (**e, f** from [34])

of CO and H₂ [33]. For the parameter variation, the authors fabricated their samples using layer-by-layer physical vapor deposition (PVD), where Au was deposited first to form small islands on the substrate and then covered with YSZ (Fig. 8.2c). They then exposed the film to different concentrations of H₂ and CO at a temperature of 500 °C and monitored the spectral changes of the film's plasmon resonance peak at a wavelength of around 580 nm. Calibration curves for several Au nanoparticle configurations are shown in Fig. 8.2d. The authors found that the film with the smallest Au particles (mean crystallite size of approx. 50 nm) yielded the largest response to hydrogen exposure (Fig. 8.2d). When comparing this response to a co-deposited nanocomposite film, where the Au particles were embedded in an YSZ matrix, they obtained an enhancement of the sensing performance by a factor of 1.5. However, this enhancement is accompanied by a decrease of the sensitivity to CO. Still, the study by Dharmalingam et al. outlines how sensitivities and selectivity in Au-YSZ nanocomposite films can be tuned by a straightforward variation of one of the structure parameters, accelerating the development of integrated sensor chips for multiple reagents.

Au-YSZ can also serve as a broader model system for the investigation of electrochemical reactions in nanocomposite geometries, as demonstrated by the work of Rogers et al. [34]. They monitored the optical response of Au nanoparticles embedded in an YSZ matrix during H₂ exposure. However, by simultaneously

tuning the concentration of H₂ and O₂, they were able to achieve much better control over the electrochemical reactions occurring in the nanocomposite film. They studied hydrogen to oxygen ratios in nitrogen carrier gas ranging from 10 (1 vol.% H₂, 0.1 vol.% O₂) to 0.005 (0.05 vol.% H₂, 10 vol.% O₂) and found a clear influence of the mixing ratio on the optical response (Fig. 8.2e). When comparing the spectral shifts in their nanocomposite system for different H₂ and O₂ concentrations, the authors made two key observations: an increase of the H₂ concentration generally led to a blueshift and a narrowing of the plasmon resonance, whereas an increase of the O₂ concentration led to a redshift and a broadening (Fig. 8.2f). This behavior could be explained by reaction-induced charge transfer between the oxygen ions in the YSZ matrix and the Au nanoparticles, where the blue- and redshifts were associated with charge injection and removal, respectively. Taking a further step, the authors were able to correlate the plasmon resonance position (and thus the square root of the charge density in the Au nanoparticles) with the gas mixture ratio through an electrochemical model, paving the way towards the all-optical interrogation of different oxygen ion transport and charge transfer mechanisms.

8.2.3 Chemical Sensing in Harsh and Corrosive Environments

In recent years, industrial energy production has experienced an increasing shift from traditional fossil-based technologies towards renewable sources. However, large-scale petrochemical processing is still a vital step in the production of a multitude of products ranging from plastics to pharmaceuticals. Many important petrochemical reactions take place at high temperatures and otherwise harsh or corrosive environments, which requires constant and reliable process monitoring. Due to their durability, sensitivity and all-optical readout, plasmonically functionalized thin films are well positioned to detect a variety of reagents in such challenging environments.

Towards this goal, Ohodnicki et al. have utilized an Au/TiO₂ nanocomposite film for the detection of hydrogen at temperatures as high as 850 °C [35]. The authors prepared their nanocomposite through sol-gel deposition techniques and obtained a TiO₂ matrix with a well-controlled amount of dispersed Au crystallites (Fig. 8.3a). TiO₂ was chosen due to its reactivity to a variety of gaseous reagents combined with excellent thermal stability. They then examined the sensing performance of their device by exposing it to 4 vol.% H₂ in N₂ carrier gas at temperatures of 600 °C and 850 °C and recording the transmittance changes close to the plasmon resonance position at a wavelength of 625 nm (Fig. 8.3b). The authors observed pronounced, reversible and reproducible transmittance changes for both temperatures and found that the response time of their system could be substantially reduced from 33 to only 3 min by increasing the temperature from 600 °C to 850 °C. This rapid and reproducible response makes the Au/TiO₂ system suitable for chemical process monitoring, especially at high temperatures associated with advanced petrochemical processing or reactions in solid oxide fuel cells.

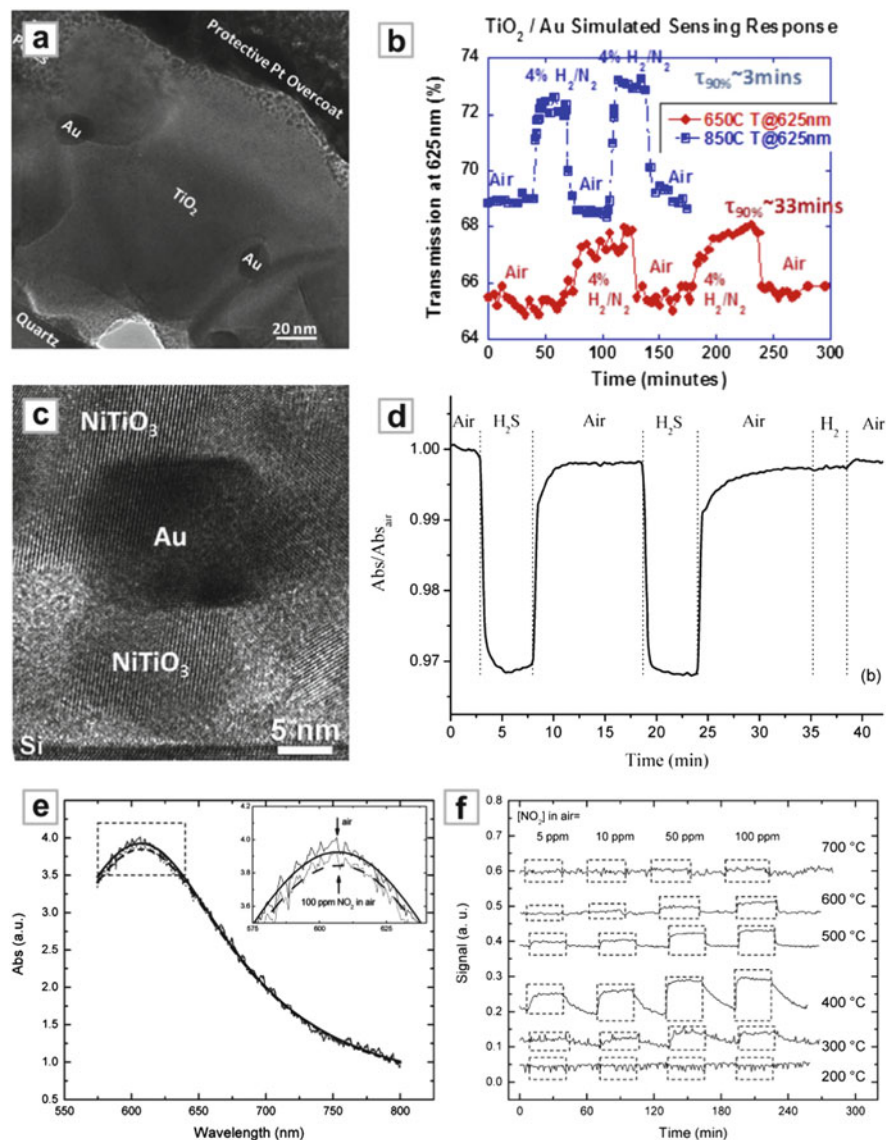


Fig. 8.3 Sensing in harsh and corrosive environments. (a) Cross-sectional TEM images for an Au/TiO₂ nanocomposite thin film. (b) Sensing response of an Au/TiO₂ film to 4 vol.% H₂ in different environmental conditions (a, b from [35]). (c) Bright-field TEM images of an Au-70TiO₂-30NiO nanocomposite film. (d) Dynamic response of the Au-TiO₂-NiO nanocomposite film to gas concentrations of 0.01 vol.% H₂S and 1 vol.% H₂ in air (c, d from [36]). (e) Absorbance spectra and Lorentzian fits for an Au-YSZ film exposed to air and 100 ppm NO₂ in air. (f) Sensor signal intensity over time for a Au-YSZ film exposed to air (signal decrease) and 5, 10, 50, and 100 ppm NO₂ in air (signal increase) at 200, 300, 400, 500, 600, and 700 °C (e, f from [37])

Besides high-temperature chemical monitoring devices, sensors for the detection of reagents in harsh or corrosive environments also play a pivotal role in controlling large-scale chemical processing plants. Hydrogen sulfide (H_2S) is a prominent example for a toxic and corrosive gas that is produced in chemical reactions ranging from natural gas manufacturing to food production. Della Gaspera et al. utilized a TiO_2 -NiO film with embedded Au nanoparticles for the detection of H_2S down to the parts per million (ppm) range [36]. The authors produced the films using a sol-gel method with a subsequent annealing step at 500–600 °C and examined three composition ratios of the TiO_2 -NiO system: 70 TiO_2 -30NiO, 50 TiO_2 -50NiO, and 30 TiO_2 -70NiO. A bright-field TEM image of an Au-70 TiO_2 -NiO nanocomposite film also showed that annealing at 600 °C could result in the formation of NiTiO_3 islands in addition to the NiO and TiO_2 phases (Fig. 8.3c). In their gas sensing experiments, the authors exposed the three nanocomposite films to 100 ppm H_2S and 1 vol.% H_2 in air and monitored the absorbance change at resonance over time (Fig. 8.3d). They found that the Au-70 TiO_2 -NiO film yielded the best dynamic behavior with large absorbance changes as well as quick response times. The sample also showed only a negligible response to H_2 versus H_2S , even at a concentration ratio of 100:1, demonstrating the excellent selectivity of the device.

So far, we have mainly covered sensing applications for chemical process engineering. However, the monitoring of exhausts released into the environment is equally important. Many combustion processes release large amounts of nitrous oxides (NO_x), which contribute to the formation of acid rain and degrade water quality on a global scale. Thus, the detection of NO_x close to the source of formation in, e.g., a turbine jet engine is crucial for the development of low-emission machinery. Here, Rogers et al. extended their previous work on Au/YSZ nanocomposites towards the detection of NO_x in small amounts and at temperatures between 500 °C and 800 °C [37]. They prepared their nanocomposite using co-magnetron PVD with a subsequent annealing step and obtained films with an average grain size of approx. 28 nm for both Au and YSZ crystallites. The film was then exposed to different ppm range concentrations of NO_2 in air and the optical absorbance change was recorded for different temperatures. When comparing the absorbance spectra for 100 ppm NO_2 in air with air at a temperature of 500 °C, a redshift and a broadening of the plasmon resonance could be observed (Fig. 8.3e). The authors attributed this behavior to the removal of electrons from the Au nanoparticles, caused by oxygen ion production during the dissociation of NO_2 on the Au-YSZ nanocomposite. To further characterize the temperature dependence of the sensor response, they exposed their sensor device to concentrations of 5, 10, 50, and 100 ppm NO_2 in air at different temperatures ranging from 200 °C to 700 °C. To simplify analysis, the authors subtracted the optical spectra during gas exposure from the “baseline” spectrum in air and defined their sensor signal as the difference between maximum and minimum of the resulting curve (Fig. 8.3e). They found the highest sensor signal change for a temperature of 400 °C whereas the best trade-off between magnitude of the signal and response time was observed at a temperature of 500 °C, with a sensitivity down to 5 ppm NO_2 in air. Furthermore, they were able to resolve

concentrations of 50 ppm NO₂ in air in a wide temperature range from 300 °C to 700 °C, which makes their design ideally suited for industrial NO₂ monitoring.

8.3 Shell-Isolated Nanoparticle-Enhanced Raman Spectroscopy

One important application of plasmonic enhancement is the amplification of Raman scattering signals from molecules adsorbed on roughened or nanostructured metallic surfaces [38]. In general, Raman spectroscopy is used to investigate rotational and vibrational transitions in molecules through the measurement of inelastically scattered photons from the sample. However, inelastic scattering signals in such systems are generally much weaker than the elastic Rayleigh scattering and thus are difficult to detect. Here, deposition of molecules onto, e.g., a roughened or nanopatterned metal film can greatly enhance the inelastic response. This signal increase can be understood in terms of surface plasmon propagation at the metal-molecule interface, which leads to strongly enhanced electromagnetic fields as well as to a chemical effect due to charge transfer complexes. Depending on the material and morphology of the substrate, surface-enhanced Raman scattering (SERS) geometries can reach enhancement factors in the 10¹⁰ range, which makes them suitable for the detection of single molecules [39].

In order to investigate the nanoscale properties of novel catalytic or reactive materials, current approaches need to be extended towards localized optical probes that can be freely dispersed on any surface or morphology, while retaining the high enhancement factors crucial for Raman scattering measurements. Li et al. have utilized small silica-coated gold nanoparticles to perform shell-isolated nanoparticle-enhanced Raman spectroscopy (SHINERS) [40]. For fabrication, the authors chemically synthesized spherical gold particles with a diameter of around 55 nm, which were subsequently coated with a thin, uniform, and optically transparent silica shell (Fig. 8.4a). The purpose of the thin shell is twofold; it offers controllable separation of the gold core from the surface to be studied as well as protection of the core from the chemical or biological environment. In addition, the amount of field-enhancement around the nanoprobe can be tailored by varying the shell thickness. The authors first applied their technique to hydrogen adsorption on platinum. They spread the shell-isolated nanoprobe on a Pt(111) single-crystal electrode covered by a 0.1 M NaClO₄ electrolyte and started the hydrogen generation reaction by applying a suitable electrode potential. Through the use of particles with an ultrathin SiO₂ shell of only 2 nm, they were able to detect the Raman signal of the adsorbed hydrogen. To further demonstrate the versatility of their approach for environmental monitoring and food safety applications, the authors studied pesticide residues on fruits. They dispersed their nanoprobe on orange skin with and without methyl parathion contamination and recorded the Raman scattering signal (Fig. 8.4c). They were able to clearly detect the presence

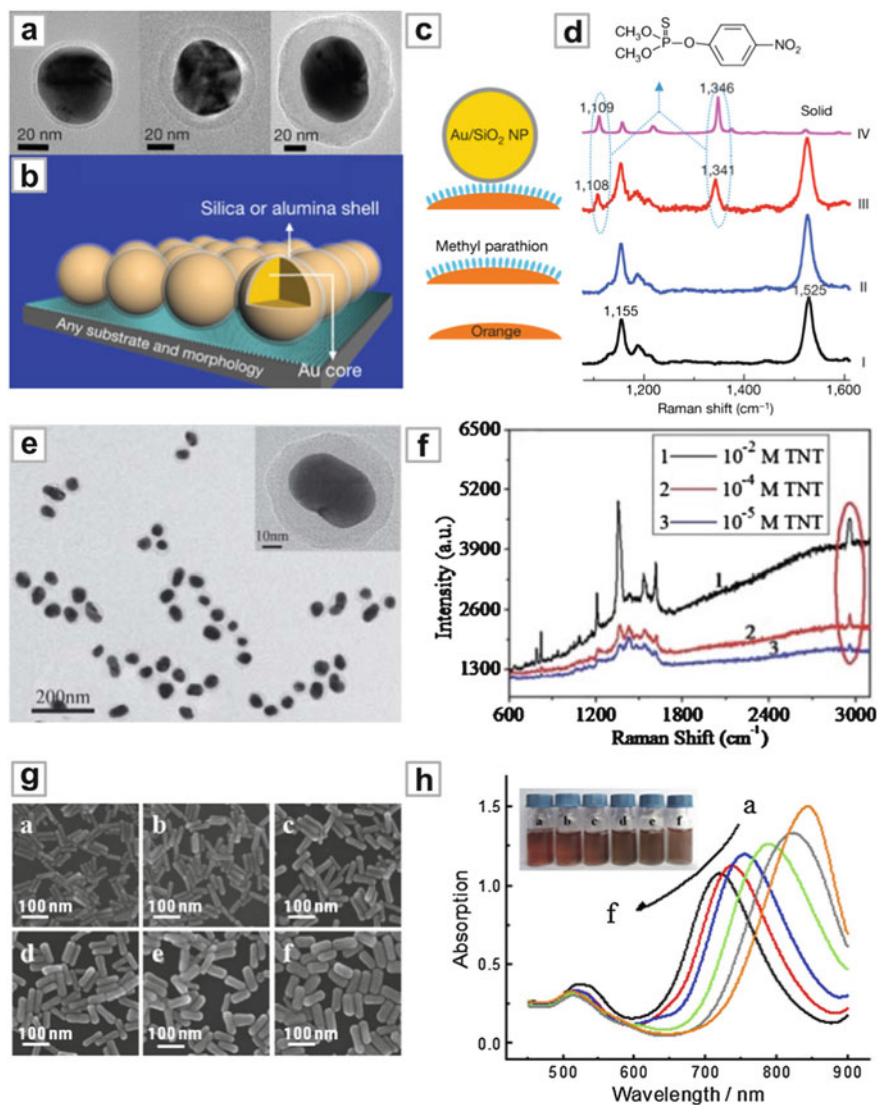


Fig. 8.4 Shell-isolated nanoparticle-enhanced Raman spectroscopy. **(a)** TEM images of Au/SiO₂ core – shell nanoparticles with different shell thicknesses. **(b)** Schematic of the sensing principle. Shell-isolated nanoparticles can be used to probe any surface or morphology. **(c)** Schematic of a SHINERS experiment for the detection of pesticides on citrus fruits. **(d)** Normal Raman and SHINERS spectra for oranges with and without pesticide contamination by parathion **(a–d)** from [40]. **(e)** TEM images of Au/PAT core – shell nanoparticles with different shell thicknesses **(f)** SERS spectra of Au@2 nm PAT NPs + TNT (10⁻² M to 10⁻⁵ M) **(e, f)** from [41]. **(g, h)** Extinction spectra and SEM images of Au NRs with different aspect ratios prepared by tuning the volumes of the Au seed solution **(g, h)** from [42]

of parathion on the orange skin samples in their nanoparticle-enhanced Raman spectra, whereas measurements without the nanoprobe yielded no signal changes (Fig. 8.4d). Thus, SHINERS offers a clear advantage in sensitivity and flexibility over standard SERS approaches and constitutes an important milestone on the pathway from plasmonically functionalized thin films to more complex sensing devices.

The reliable monitoring of environmental safety is a major area of chemical sensing. One crucial aspect for land and air traveling is the detection of explosive materials in low amounts and on diverse surfaces and morphologies. To achieve this, Qian et al. demonstrated the use of functionalized shell-isolated nanoprobe for the selective detection of trinitrotoluene (TNT) [41]. They first synthesized gold nanoparticles with a diameter of 50 nm, which were then coated with an ultrathin 2 nm shell of poly-(2-aminothiophenol) (PAT). In a final processing step, the PAT was functionalized with amino groups to facilitate the binding of TNT. This resulted in uniform nanoprobe with high yield and controllable shell thickness (Fig. 8.4e). The authors then performed SHINERS measurements on their nanoprobe in the presence of different amounts of TNT ranging from 10^{-2} to 10^{-5} M and observed several TNT-specific Raman peaks in their spectra for all concentrations (Fig. 8.4f). To elucidate the mechanism for the TNT-PAT binding, the authors focused on the Raman peak around $2,955\text{ cm}^{-1}$, which they attributed to the formation of a Meisenheimer complex between the TNT molecules and the amino groups at the PAT surface. By tracking signal changes only at the wavenumber associated with the highly specific Meisenheimer complex, the authors were able to demonstrate excellent selectivity of their sensor geometry even when exposed to very similar reagents such as dinitrotoluene (DNT).

To optimize the sensing performance of SHINERS-based devices even further, more complex particle geometries with tunable properties need to be synthesized. In this context, Zhang et al. investigated gold nanorods covered with an ultrathin shell of silica [42]. By varying the amount of gold seed solution in their synthesis process, they were able to reproducibly grow nanorods with different lengths and aspect ratios ranging from 2.2 to 3.7 (Fig. 8.4g). In addition, the shell thickness could be varied from 3 to 7 nm. To optically characterize their shell-isolated nanoparticles, the authors performed absorbance measurements and found that the plasmon resonance wavelength of their nanoprobe could be tuned from around 700 nm well beyond 800 nm (Fig. 8.4h). With such flexibility, SHINERS-based sensor geometries can easily be tuned to the wavelength of an exciting laser beam, maximizing the Raman enhancement and allowing for reagent detection with greatly improved sensitivity.

8.4 Label-Free Refractive Index Gas Sensing

Many of the sensing approaches presented so far have relied on a combination of passive plasmonic antennas, often composed of noble-metal nanoparticles, with a chemically active surrounding material. This material allows the composite system

to exhibit selectivity to specific reagents and provides a reactor for chemical surface or bulk processes. Label-free sensing devices, on the other hand, focus on the reagent-induced refractive index changes in the vicinity of plasmonic structures. Since the adsorption of biological molecules or the generation of new compounds in chemical processes causes fairly large refractive index changes, label-free methods are well suited for the investigation of a plethora of liquid-phase systems [43]. However, the label-free detection of chemical reagents and processes in the gaseous phase is significantly more challenging, mainly due to the minute refractive index changes associated with gas concentration variations.

Bingham et al. utilized high-resolution localized surface plasmon resonance (HR-LSPR) spectroscopy on arrays of silver nanoparticles to detect gas-induced refractive index changes in the 10^{-4} range (Fig. 8.5a) [44]. For their gas sensing experiments, the authors fabricated Ag nanoparticle arrays using nanosphere lithography and recorded extinction spectra while alternating the gaseous environment

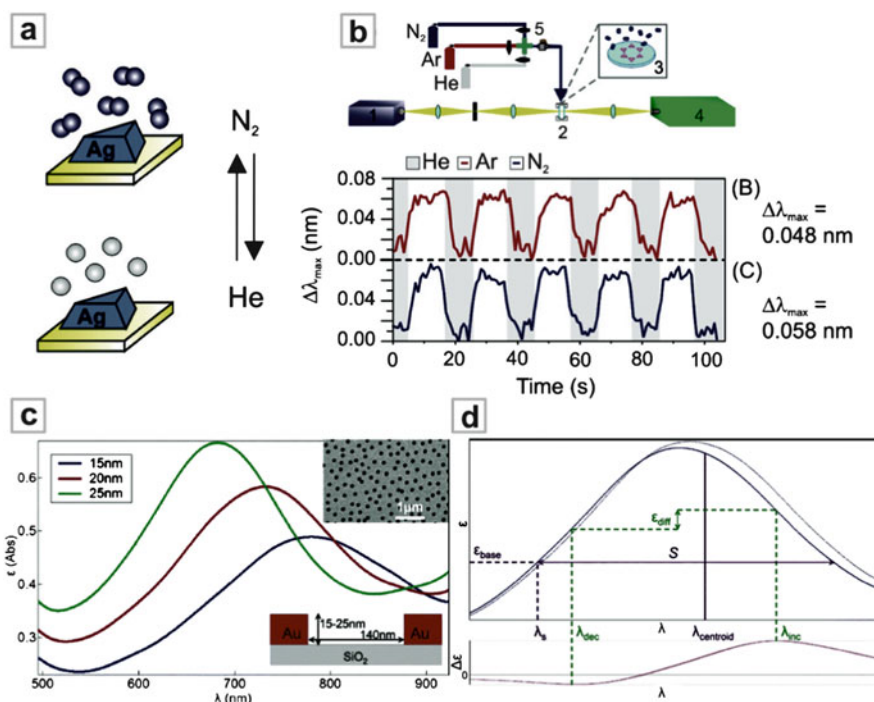


Fig. 8.5 Sensitive reagent detection using high-resolution LSPR spectroscopy. (a) Refractive index gas sensing with silver nanoparticles. (b) Resonance position of the Ag nanoparticles over time as the gas switches between He/Ar and He/N₂ (a, b from [44]). (c) Extinction spectra of 140 nm-wide nanoholes with constant surface density ($\sim 9 \mu\text{m}^{-2}$) but different depths. (d) Illustration of the parameters used in the centroid detection algorithm using a typical nanohole LSPR peak before and after a small increment in bulk RI. Shown below is the difference between the two spectra. The parameters used to analyze the peak position, centroid wavelength $\lambda_{\text{centroid}}$, centroid span S , and baseline intensity ϵ_{base} , are indicated (c, d from [45])

repeatedly between helium/argon and helium/nitrogen every 10 s. They observed clear spectral redshifts when switching from He to the target gases, with magnitudes of 0.048 nm and 0.058 nm for Ar and N₂, respectively, which corresponds to a sensitivity of around 200 nm/RIU. In addition, the authors performed gas exchanges every 5 s and again found mass-transport limited rise and fall times, indicating the detection of RI changes in the gaseous environment as opposed to adsorption processes at the Ag surface. The main enabling factors in their high-resolution measurements were the use of silver for plasmonic resonators with low intrinsic damping, the stability of their experimental setup, and the ability to precisely track the plasmon resonance wavelength over multiple measurements.

A reliable and highly accurate technique for determination of the resonance position from (potentially noisy) experimental spectra is the centroid method as introduced by Dahlin et al. for LSPR spectroscopy [45]. As a first application, the authors investigated the sensitivity of nanohole arrays in a thin gold film towards small refractive index changes in the environment (Fig. 8.5c). The centroid method relies on the computation of the first moment (or center of mass) of a spectral intensity distribution $I(\lambda)$, taken over a certain wavelength span S (Fig. 8.5d). In order to reduce measurement noise and provide a continuous analytical representation of the experimental data, the authors first fitted the nanohole absorbance spectra $I(\lambda)$ using a high-degree polynomial $\varepsilon(\lambda)$ of order 20. The starting wavelength λ_s of the span S in the spectra was obtained by minimizing the expression $\varepsilon(\lambda_s + S) - \varepsilon(\lambda_s)$ and the intensity baseline $\varepsilon_{\text{base}}$ was defined as $\varepsilon(\lambda_s)$. The centroid wavelength $\lambda_{\text{centroid}}$ was then calculated using

$$\lambda_{\text{centroid}} = \frac{\int_{\lambda_s}^{\lambda_s+S} \lambda (\varepsilon(\lambda) - \varepsilon_{\text{base}}) d\lambda}{\int_{\lambda_s}^{\lambda_s+S} (\varepsilon(\lambda) - \varepsilon_{\text{base}}) d\lambda}$$

Since there is a linear relationship between the resonance wavelength λ_{peak} and $\lambda_{\text{centroid}}$ with a proportionality factor of roughly 1 for most plasmonic systems, the centroid wavelength shift serves as a reliable measure for sensor performance. Overall, the centroid detection approach allows for the sensitive, robust and reproducible extraction of resonance wavelength positions from noisy experimental data and thus enables a plethora of applications in biological and chemical sensing. In this, it is clearly superior to common peak tracking or fitting methods due to the inclusion of the full span S of spectral data and its suitability for, e.g., non-Lorentzian line shapes.

8.5 Engineered Nanoparticles and Smart Dust

Highly engineered or “smart dust” nanoparticles offer many exciting possibilities for the detection of chemical or biological reagents [46]. Furthermore, the combination of multiple materials in complex core-shell nanoparticles and the use of advanced

synthesis procedures allow for new functionalities as well as increased flexibility in structure design [47–49]. Implementing this concept for plasmonic gas sensing, Ghodselahi et al. have demonstrated the use of Cu@CuO core-shell nanoparticles for the detection of carbon monoxide [50]. The authors first prepared hexagonal Cu nanoparticle arrays on a glass substrate using codeposition of RF-sputtering and RF-PECVD, and subsequently oxidized them under airflow to obtain the CuO shell structure. This yielded uniform Cu@CuO core-shell nanoparticles with a thickness of 35 nm and a mean lateral dimension of 10 nm. To demonstrate the carbon monoxide sensitivity of their system, the authors recorded absorbance spectra of their sample during exposure to different flow rates of CO. In ambient air, they observed a pronounced plasmon resonance peak at around 600 nm, which underwent a spectral redshift and an increase in the absorbance for increasing CO flow rate (Fig. 8.6a). Spectral redshifts of approx. 3 nm were observed for a low flow rate of 1.6 l/h, with a maximum value of approx. 8 nm and saturation-like behavior for flow rates in the 10 l/h range (Fig. 8.6b). This response could be attributed to CO adsorption on the CuO shell, which leads to a dielectric change in the active material and thus to a spectral shift of the plasmon resonance in the Cu. Since CO molecules are only adsorbed on the particle surface, the CuO shell could potentially be cleaned via a low-temperature annealing step in air. This would reduce sensor performance degradation and enable long-term environmental monitoring applications.

Apart from different metals and oxides, smart dust nanoparticles can also be capped with biological species to facilitate the detection of diverse reagents. Vasileva et al. have demonstrated the use of starch-stabilized silver nanoparticles to detect hydrogen peroxide (H₂O₂) [51]. Hydrogen peroxide plays an important role in the human body, where it is a key factor for oxygen metabolism, enzymatic breakdown of glucose or lactose, and oxidative stress [52]. In their experiments, the authors designed a green synthesis procedure employing only soluble starch, silver nitrate, D-glucose, and sodium hydroxide to obtain an aqueous dispersion of nanoparticles with a mean diameter of 14.4 nm and excellent uniformity. Importantly, they performed ultrasonication and controlled alkalization of the reaction medium to tailor the size and shape of their Ag particles (Fig. 8.6c). A key feature of their synthesis approach is the use of soluble starch as a capping agent, which eliminated the need for toxic chemicals in the reaction process and still allowed for sufficient control over particle morphology. When added to the nanoparticle dispersion, H₂O₂ acted as an active oxidant, leading to the degradation of the starch-stabilized silver particles. The authors could correlate this degradation with the absorbance strength of the silver particles' plasmon resonance and thus were able to reliably differentiate H₂O₂ concentrations ranging from 10⁻¹ to 10⁻⁶ mol/l (Fig. 8.6d).

A different bio-inspired approach for detection of H₂O₂ has been demonstrated by Endo et al. [53]. They used silver nanoparticles in solution to obtain a pronounced plasmonic response, but coated them with polyvinylpyrrolidone (PVP) to improve their stability towards other reagents (Fig. 8.6e). Exposure to H₂O₂ led to an aggregation of the PVP-coated Ag nanoparticles and a subsequent decrease of the

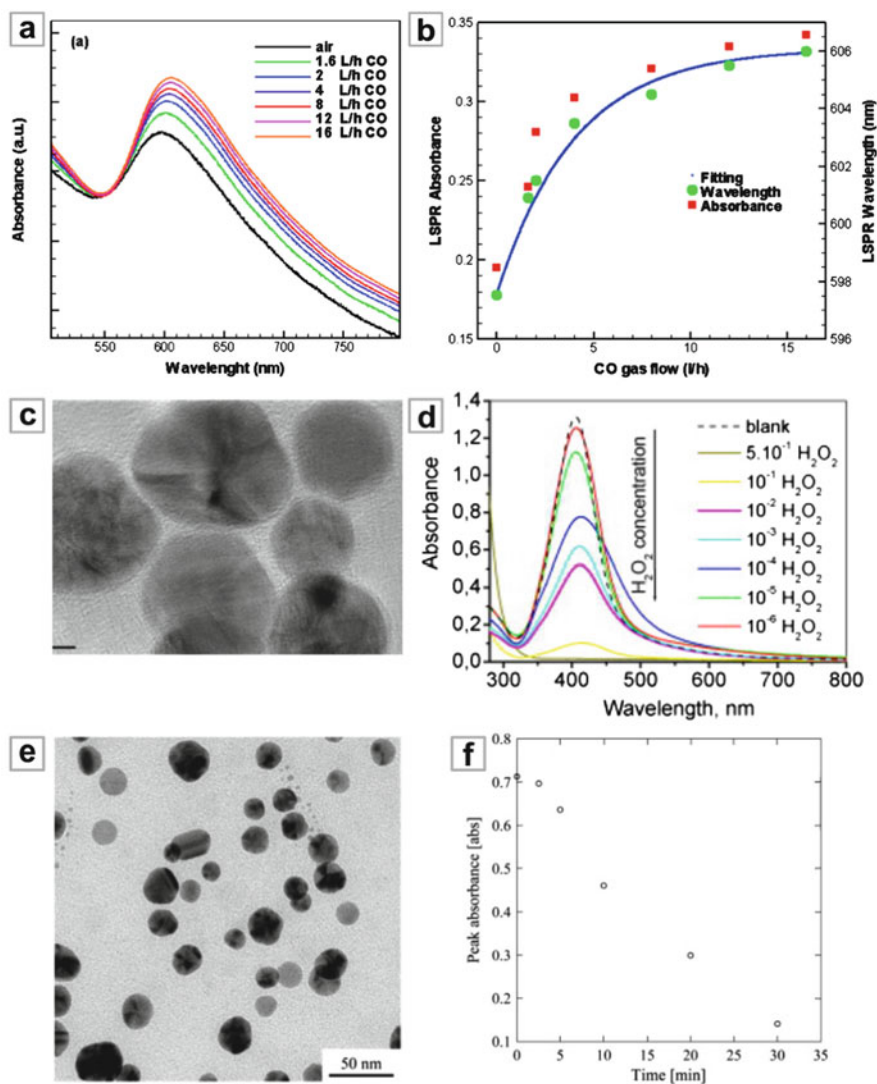


Fig. 8.6 Sensing with complex core-shell nanoparticles. (a) Absorbance spectra of Cu@CuO core-shell nanoparticles under air and various CO gas concentrations. (b) LSPR absorbance (*left*) and LSPR wavelength (*right*) versus CO concentration (a, b from [50]). (c) TEM image of starch-stabilized silver nanoparticles for hydrogen peroxide detection. (d) Absorbance spectra of the Ag nanoparticle solution 15 min after the addition of hydrogen peroxide solution for different H₂O₂ concentrations (c, d from [51]). (e) TEM image of polyvinylpyrrolidone-coated silver nanoparticles in water. (f) Absorbance at resonance over time after the addition of 1 mM hydrogen peroxide (e, f from [53])

absorbance strength of the plasmon resonance at a wavelength of around 405 nm. The authors investigated this behavior in more detail by introducing 1 mM H_2O_2 into a vial of PVP-coated Ag nanoparticles and tracking the absorbance over time (Fig. 8.6f). They again observed a strong decrease of the peak absorbance, with a large enough effect to be visible by naked eye. Thus, such coated nanoparticles could be employed as cheap and biocompatible color markers for medical and pharmaceutical applications.

Due to their unique properties, plasmonic smart dust particles can sensitively probe localized structural features such as size, shape, material, and morphology [54, 55]. Furthermore, the efficiency of many physical, chemical and catalytic processes depends crucially on such nanoscale properties. This is especially true for large-scale catalytic hydrogen generation and storage, which are a key component of green energy production and may facilitate a move away from present, fossil-based technologies.

Palladium constitutes an ideal model system for hydrogen dissociation and subsequent absorption processes in metals [56–59]. During catalytic loading, hydrogen molecules are first chemisorbed on the Pd surface, followed by near barrierless dissociation and subsequent diffusion of atomic hydrogen into the lattice. When increasing the hydrogen concentration, palladium undergoes a phase transition from a mobile, solid solution α -phase to a palladium hydride (PdH) β -phase. This transition causes both an expansion of the Pd lattice as well as a pronounced change in the dielectric function.

To study the influence of the localized particle geometry on this reaction, Tang et al. investigated the hydrogen uptake trajectories for individual Au/Pd core-shell particles with different shapes, faceting, and Pd shell thickness [60]. The authors employed a synthesis method designed for particles with high quality but low uniformity to obtain a mixture of triangular plates, decahedrons, and icosahedrons (Fig. 8.7a). This allowed them to study nanoparticles with different sizes and shapes from the same synthesis process, aiding in reproducibility. The authors first studied hydrogen-induced shifts of the plasmon resonance for an Au/Pd core-shell triangular plate and found a pronounced spectral redshift on the order of 25 nm (Fig. 8.7b). Both this result and similar measurements on icosahedrons were found to be in good agreement with numerical simulations, taking into account the dielectric function change from Pd to PdH. However, when investigating decahedral nanoparticles, the authors measured a pronounced spectral blueshift upon initial H_2 exposure (Fig. 8.7b), which could not be accounted for in numerical simulations using a simple Pd/PdH transition. This contrasting behavior was attributed to two chemical transformations that occur during hydrogen exposure: the interdiffusion of Au and Pd, which leads to an effective decrease of the Au particle size and thus a blueshift, and the formation of palladium silicide due to a reaction of the nanoparticles with silicon atoms of the substrate below. Both effects were found to be especially pronounced in nanoparticles with thicker Pd shells, allowing for the straightforward differentiation of the particle species. Thus, the plasmonic resonance of individual smart dust nanoparticles can serve as a sensitive probe for H_2 storage properties and metal support interactions in nanocatalytic systems, revealing geometry-dependent properties that are not accessible via standard ensemble measurements.

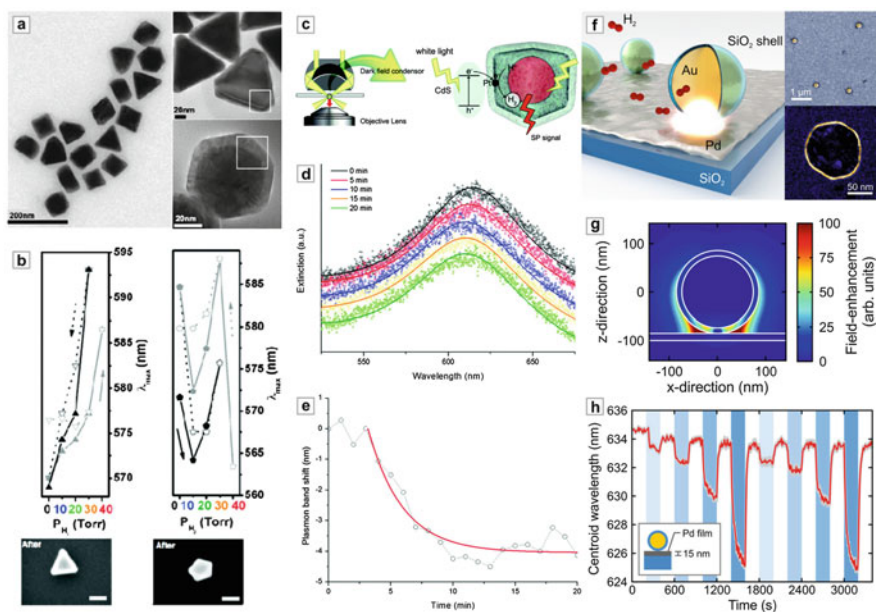


Fig. 8.7 Complex smart dust nanoparticles for hydrogen and chemical sensing. (a) Low- and high-resolution TEM images of Au/Pd core-shell nanocrystals (b) Plasmon resonance shift upon hydrogen uptake and release for a single Au/Pd core-shell triangular plate (left) and decahedron (right) (a, b from [60]). (c) Schematic diagram of single-particle measurement and detection on a single Au@Pt/CdS catalyst particle. (d) Extinction spectra of a single Au@Pt/CdS cube along the reaction progress. (e) Plasmon resonance shift during reaction for the same cube (c–e from [61]). (f) Schematic of plasmonic probing of local chemical reactions using smart dust nanoparticles (left). Exemplary element-resolved TEM and SEM images of the probing platform (right). (g) Electric near-field distribution at resonance. The intense near-fields are strongly localized at the touching point between the smart dust particle and the Pd film. (g) Time-resolved centroid wavelengths in response to hydrogen uptake and release for a single smart dust particle on a 15 nm Pd film (f–h from [62])

An ideal application for such smart dust nanoprobe is the catalytic generation of hydrogen, which is a key prerequisite for renewable energy production. Here, Seo et al. investigated the photocatalytic decomposition of lactic acid for hydrogen generation, using platinumized cadmium sulfide (Pt/CdS) nanocubes [61]. In order to enable in-situ monitoring of the produced H₂ gas, they integrated gold domains into the nanocube reactors and recorded time-resolved dark-field scattering spectra from single structures (Fig. 8.7c). When their nanoreactors were illuminated with white light, photons that match the optical band gap were absorbed in the CdS shells, leading to the generation of photoelectrons. These electrons can transfer to the Pt part and react with protons from the surrounding solution to produce H₂ gas. During the reaction, the authors observed a gradual blueshift of the plasmonic resonance with a maximum value of 14 nm combined with a decrease of the scattering amplitude (Fig. 8.7d). This was found to be consistent with a change of the local environment close to the gold probe from 10 % lactic acid in water ($n = 1.342$)

to hydrogen gas ($n = 1.000$), taking into account that the Au probe has an average distance of 20 nm from the active Pt surface. As expected, the time-resolved spectral resonance position followed a saturation behavior, reaching the maximum blueshift after around 10 min (Fig. 8.7e). By performing further analysis on their spectral time trace data, the authors were able to estimate the hydrogen generation from a single nanoreactor particle at around 1,300 molecules per minute, showing that the use of smart dust probes can yield detailed information on local reaction kinetics from non-invasive far-field measurements.

In order to extend the presented concepts to the detection of chemical or catalytic processes in realistic material systems and environmental conditions, there is a need for a versatile sensing platform that can probe arbitrary surfaces and morphologies. To achieve this, Tittl et al. utilized silica shell-isolated gold nanoparticles to monitor local chemical reactions in real time [62]. The smart dust nanoparticles can focus incident light into subwavelength hot spots of the electromagnetic field and optically report minute environmental changes at their pinning sites on the probed surface during reaction processes (Fig. 8.7f, left). Furthermore, the smart dust particles can easily be dispersed on target surfaces via drop-coating and allow for straightforward all-optical readout via standard dark-field spectroscopy (Fig. 8.7f, right). As a model system, the authors investigated the hydrogen dissociation and subsequent absorption in adjacent palladium thin films. A key feature of their particles is the ultrathin SiO₂ shell with a thickness of 10 nm (Fig. 8.7f, right), which both separates the Au core from direct contact with the probed agents and enables the high localized field-enhancements necessary for the sensitive detection of dielectric changes in the neighboring Pd film (Fig. 8.7g). For their sensing measurements, the authors exposed a “dust on film” sample consisting of smart dust nanoprobos on a 15 nm Pd film to concentrations of 0.5, 1, 2, and 3 vol.% hydrogen in nitrogen carrier gas. They were able to observe different concentration steps as clear spectral blueshifts in the optical scattering response of single smart dust particles, with a maximum value of around 8 nm for 3 % H₂ (Fig. 8.7h). To check the ability of their platform to resolve localized morphology changes, the authors next investigated the “film on dust” system, where the smart dust particles were covered with a highly curved Pd film via tilted angle evaporation and found pronounced redshifts for all concentrations. This shows how the smart dust probing platform can transform small localized morphology changes into a complete reversal of the spectral shift direction in the far-field optical response, allowing it to resolve chemical reactions for nearly arbitrary material placements and configurations. In the future, such techniques could combine two-dimensional imaging and spectroscopy to locally map chemical and catalytic reactions on a subdiffraction-limit scale.

8.6 Large-Area Nanostructured Sensor Chips

Synthesis and deposition-based approaches enable the reliable and high-throughput fabrication of plasmonic nanosensor devices. However, in order to produce large-area sensor chips with a predefined spatial arrangement of plasmonic elements, other

fabrication methods such as soft-imprint lithography, nanosphere lithography, or (to some extent) electron-beam lithography often need to be implemented [5, 6].

As a first example of nanosphere lithography, Wang et al. utilized ordered gold nanoparticle arrays to study the chemical adsorption of mercury vapor on the Au surface [63]. They fabricated the particle arrays by evaporating 2 nm chromium (Cr) and 40 nm Au through the interstitial voids of a densely packed monolayer of polystyrene (PS) nanospheres, followed by sonication in ethanol to remove the PS spheres from the substrate. This yielded triangular gold nanoparticles with a hexagonal spatial arrangement, which could be transformed into more circular nanodisks by a subsequent annealing step (Fig. 8.8a). The authors then exposed their sample to 15 ppm of mercury vapor delivered by nitrogen flow and monitored the shift of the plasmon resonance peak over time. They found a clear monotonic spectral blueshift from 565 to 560 nm, which saturated after 2 h and reached 85 % of the maximum value after around 30 min (Fig. 8.8b). This adsorption time was found to be shorter than in the case of an extended Au film, where only 67 % of the maximum response was obtained after 30 min [64]. In addition, the authors were able to regenerate their sensor chip using a heating step at 300 °C for 30 min, resulting in a return of the plasmon resonance position to the original value. The blueshift was attributed to the formation of an adsorbed mercury shell on the hemispherical Au nanoparticles, which could be clearly observed as a volume increase in AFM measurements, leading to a change of the effective refractive index and thus the observed spectral shifts.

Ma et al. used a structurally similar system for the detection of chloroform vapor, a prime example of volatile organic compounds (VOC) that play a role in both industry and medical diagnostics [65, 66]. Their sensor device consisted of an array of triangular silver nanoparticles, covered with a layer of poly(methyl methacrylate) (PMMA) transduction layer which provided the reagent sensitivity [67]. For fabrication, the authors utilized nanosphere lithography followed by spin-coating of the PMMA layer to produce high-quality ordered nanoparticle arrays over large areas (Fig. 8.8c). PMMA was chosen as a chloroform sensitive material due to its excellent long-term stability, low optical loss and transparency in the visible spectrum. In optical extinction measurements, the system exhibited a clear plasmon resonance at a wavelength of around 670 nm, which decreased in magnitude upon exposure to increasing concentrations of chloroform vapor (Fig. 8.8d). Compared to this pronounced response in extinction magnitude, the authors found only small changes in the resonance wavelength for the different chloroform concentrations. This spectral behavior was found to be consistent with chloroform-induced swelling in the PMMA layer. When switching on the chloroform vapor flow, the system reached the saturated value of maximum extinction change after a fast response time on the order of 10 s and the system returned to the initial state 300 s after switching off the flow. Finally, the authors examined the cross-sensitivity of their sensor device and found only negligible responses for exposures to benzene, toluene, ethanol, propyl alcohol, or hexane. This shows that their system can be utilized as a stable, reliable, and selective chloroform sensor for health and safety or industrial uses.

One key application of large-area nanostructured sensor chips was first demonstrated by Langhammer et al. who utilized palladium nanodisks to perform hydrogen

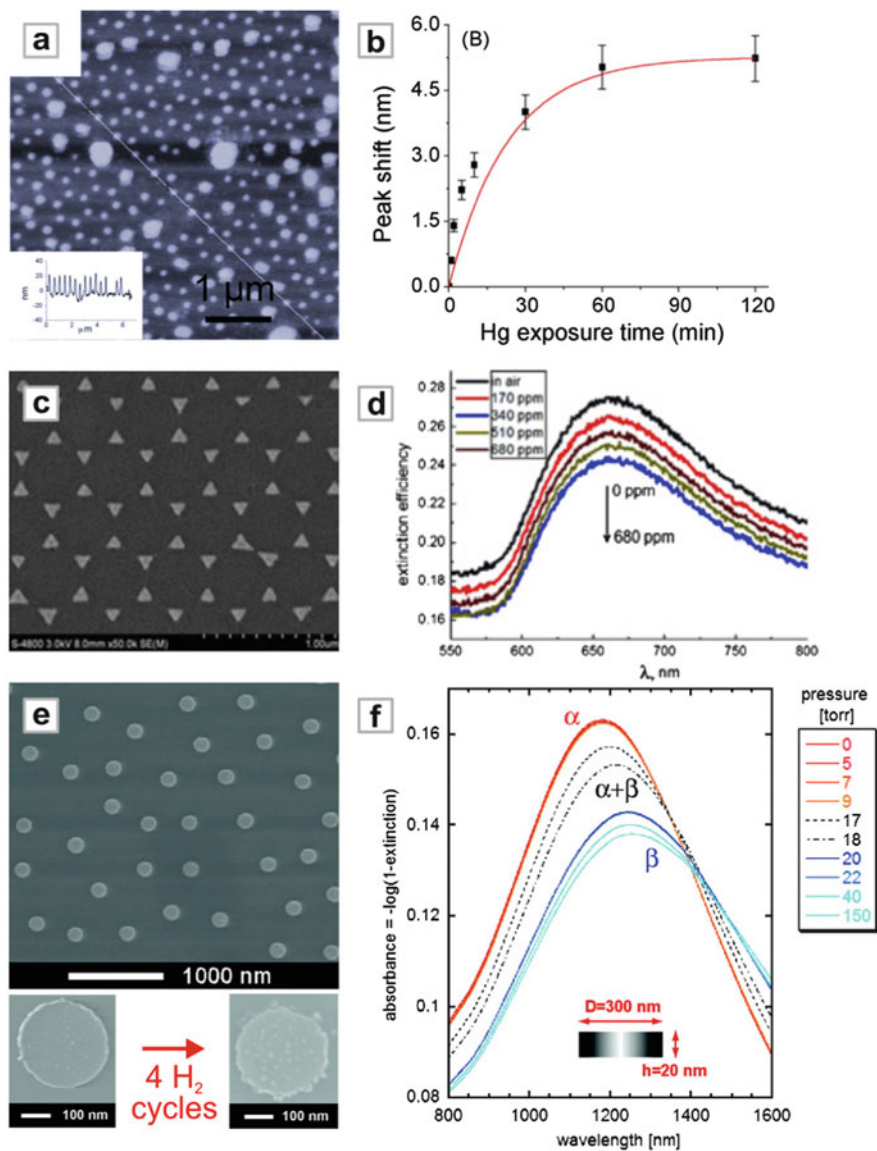


Fig. 8.8 Large-area nanostructured sensor chips. **(a)** AFM image of ordered gold nanoparticle arrays prepared using nanosphere lithography. **(b)** Plasmon resonance wavelength shifts of the gold nanoparticle arrays at different times after exposure to mercury vapor (**a, b** from [63]). **(c)** SEM image of plasmonic nanostructures coated with a PMMA transduction film. **(d)** LSPR spectral response of the PMMA-coated structures to chloroform of different concentrations (**c, d** from [67]). **(e)** SEM image of a Pd nanodisk array used for hydrogen sensing (*top*) and degradation of the system after several exposure cycles (*bottom*). **(f)** Series of measured extinction spectra for the nanodisk array at successively higher hydrogen pressures (**e, f** from [68])

sensing experiments and to study the hydrogen-induced phase transition from palladium (Pd) to palladium hydride (PdH) on the nanoscale [68]. The Pd/PdH transition causes both a strong change of the dielectric function and an expansion of the Pd lattice, allowing it to be observed in resonant plasmonic systems. To achieve this, the authors fabricated a disordered array of supported Pd nanodisks with a diameter of 300 nm using hole-mask colloidal lithography (Fig. 8.8e, top). They then measured extinction spectra for different hydrogen partial pressures ranging from 0 to 150 Torr. The initial plasmon resonance peak at a wavelength of around 1,200 nm underwent a pronounced redshift as well as a broadening and a decrease of the total extinction cross-section for increasing hydrogen pressure (Fig. 8.3f). By correlating the peak shifts with the hydrogen partial pressures, the authors were able to obtain hydrogen absorption and desorption trajectories comparable to the well-know pressure-composition isotherms that characterize the phase transition in the Pd-H system, showing that the nanoscale phase behavior can be effectively retrieved from optical measurements. They also found that it was crucial to use relative spectral shifts instead of absolute peak positions for the derivation of the pressure-composition isotherms, since repeated hydrogen loading and unloading cycles led to irreversible changes in the Pd nanostructures (Fig. 8.8e, bottom). These changes are due to the phase-transition-induced 10 % volume increase of the Pd lattice and the associated mechanical stress [56]. For use in highly stable industrial sensor devices, this hydrogen-induced structural deterioration can be overcome by, e.g., alloying Pd with nickel (Ni) and by sandwiching the resulting material in between optimized capping and buffering layers [69].

The presented nanostructured sensor chips exhibit excellent homogeneity over large areas as well as high performance and can thus serve as the reagent-sensitive element in simple, all-optical, and industry-compatible sensor devices. This enables their use in a variety of applications, especially in the field of environmental monitoring, where high numbers of sensor devices are needed.

8.7 Complex Grating-Based Plasmonic Hydrogen Sensors

In order to further improve the performance of plasmonic sensor devices, many recent designs have moved from simple plasmonic resonators towards complex coupled or hybrid nanostructures [16, 70–72]. Coupled plasmonic systems provide a way to tackle two main limiting factors for the sensitivity of such devices: the linewidth (and thus the quality factor) of the plasmon peak and the background signal close to the resonance position.

One approach to reduce the resonance linewidth is to place an array of plasmonic nanowires on top of a photonic waveguide to form a metallic photonic crystal slab [73–76]. To obtain sensing functionality, Christ et al. used Au nanowires on top of a gasochromic WO_3 waveguide, which undergoes a strong modification of its optical properties when exposed to hydrogen gas [77]. The authors also incorporated an

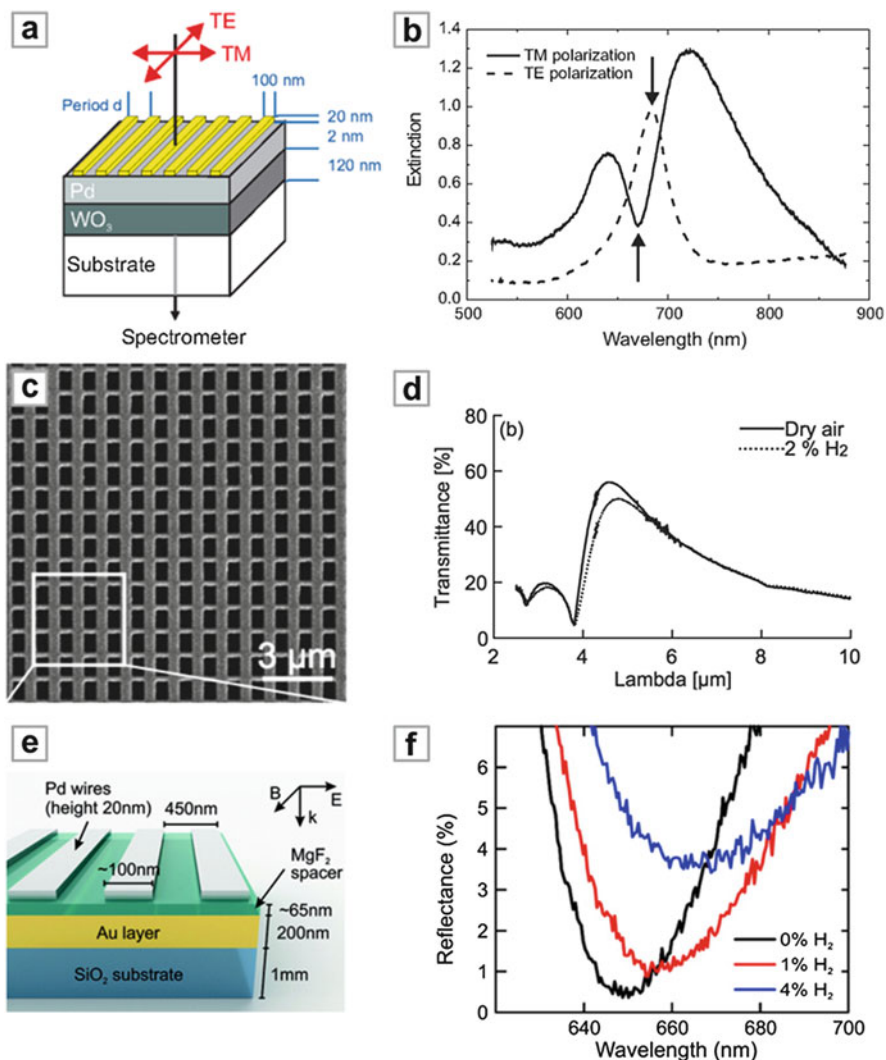


Fig. 8.9 Metallic photonic crystal and perfect absorber hydrogen sensors. (a) Schematic of a metallic photonic crystal slab which incorporates WO_3 as the waveguide layer material. (b) Extinction spectra of the photonic crystal sensor in TE and TM polarization (a, b from [77]). (c) SEM image of a subwavelength Pd hole array. (d) Transmittance change for a hole array with an aspect ratio of 1.6 when exposed to 2 vol.% H_2 in dry air (c, d from [81]). (e) Schematic of the palladium-based perfect absorber hydrogen sensor. (f) Reflectance spectra of an optimized perfect absorber structure in N_2 and when exposed to 1 and 4 vol.% H_2 in N_2 (e, f from [86])

ultrathin (2 nm) catalytic Pd layer between the wires and the waveguide to facilitate the splitting of molecular hydrogen gas into atomic hydrogen for diffusion into the WO_3 waveguide (Fig. 8.9a). When the system is excited perpendicular to the nanowires, the associated plasmon resonance can couple to the quasiguided mode of

the WO_3 waveguide, resulting in the formation of a polariton-type coupled system. In extinction measurements, the upper and lower branch of the polariton can be associated with two pronounced maxima in the spectrum. Additionally, the coupling between the broad plasmon peak and the narrow waveguide mode leads to the formation of a sharp extinction dip between the maxima, which is ideally suited for sensing due to its low FWHM (Fig. 8.9b). Upon hydrogen exposure, the optical properties of the WO_3 layer change drastically, which in turn causes pronounced changes in the extinction spectrum of the complete metallic photonic crystal slab. In their sensing experiments, the authors exposed their sample to a constant gas flow with a predefined ratio of H_2 to N_2 flow rates, allowing them to precisely set the hydrogen concentration. Extinction measurements were taken 100 s after each change of the H_2 concentration to allow the system to reach equilibrium. In TM polarization, the authors observed a pronounced response of the extinction dip at a wavelength of 674 nm when going from 0 to 20 vol.% H_2 , with an extinction change of 247 % and a resonance blueshift of 13 nm. These results exemplify how the combination of a chemically sensitive waveguide with plasmonic elements can lead to versatile and high-performance sensor geometries. Furthermore, by replacing the Au nanowires with other reactive materials, metallic photonic crystal devices can be expanded to detect two reagents simultaneously, enabling rapid multiplexing.

A different way to obtain narrow spectral features suitable for sensing applications is the coupling of incident light to an array of apertures in an optically thick metal film. In optimized geometries, this leads to a transmittance much greater than predicted from classical aperture theory, a phenomenon known as extraordinary optical transmission (EOT) [78–80]. In this context, Maeda et al. utilized the infrared transmittance through an array of rectangular subwavelength holes in a palladium film to sensitively detect hydrogen [81]. The structures were fabricated using electron-beam lithography, metal sputtering, and wet-chemical lift-off to produce hole arrays with a periodicity of 1.1 μm , a length of 0.8 μm , and varying aspect ratios (length/width) from 1 to 2.6 (Fig. 8.9c, aspect ratio 1.6). In Fourier-transform infrared (FTIR) measurements, the authors found a pronounced transmittance peak that could be tuned from a wavelength of 4 μm up to 5 μm with increasing aspect ratio. Upon exposure to a concentration of 2 vol.% hydrogen, they observed a decrease of the transmittance as well as a spectral redshift of 0.2 μm for a fabricated hole array with an optimal aspect ratio of 1.6. This behavior was confirmed by numerical simulations of the sensing performance, which included both the dielectric change associated with the Pd/PdH transition and the hydrogen-induced expansion of the Pd lattice. The authors were able to reproduce the plasmon resonance positions for all experimental values of the aspect ratio and found spectral redshifts for both the dielectric change and the lattice expansion, adding up to a total redshift consistent with the experimental data. This shows that, compared to simple Pd patches, the use of EOT structures can provide sharp spectral features with large reagent-specific responses and can thus enable highly sensitive sensor devices.

Plasmonic perfect absorber structures, designed to fully absorb incident light of a certain predefined wavelength, can be utilized to reduce the background signals commonly associated with intensity-based sensing approaches [82–85]. This

concept was applied to gas sensing by Tittl et al. who utilized a palladium-based perfect absorber structure to detect hydrogen [86]. Their system consisted of an array of Pd nanowires stacked above a dielectric (MgF_2) spacer layer and a gold mirror, which ensures zero transmittance through the structure (Fig. 8.9e). Incident light perpendicular to the wires can excite plasmon oscillations, which in turn cause the oscillation of a mirror plasmon in the thick gold film below. Ideally, these two charge distributions oscillate in antiphase to produce a circular current with an associated magnetic mode. By carefully tuning the width of the Pd wires and the height of the dielectric spacer layer, the authors were able to tailor both the effective electric permittivity ε and the magnetic permeability μ of their structure. This enabled them to match the optical impedance $z = \sqrt{\mu/\varepsilon}$ of the coupled system to the vacuum value, resulting in zero reflectance and thus an absorbance of unity. Following a numerical optimization of the design, the structures were fabricated using electron-beam lithography, thermal evaporation, and wet-chemical lift-off. In optical measurements, the authors observed a pronounced reflectance dip with a minimum value of $R_0 = 0.5\%$ at the resonance wavelength of $\lambda_0 = 650\text{ nm}$, which corresponds to an absorbance $>99\%$. Exposure of this sample to 1 and 4 vol.% H_2 in N_2 carrier gas led to a strong increase of the reflectance at resonance combined with a spectral redshift (Fig. 8.9f). For the 4 vol.% concentration, which constitutes the explosion threshold of hydrogen in air, a maximum reflectance value of 4.9% at λ_0 and a spectral redshift of 19 nm were observed. Since the reflectance at resonance is practically zero, this translated to a very large relative reflectivity change of $\Delta R_{rel} = (R_{H_2} - R_0)/R_0 = 8.8$, an increase of one order of magnitude over conventional thin-film geometries [87].

8.8 Antenna-Enhanced Sensor Geometries

Plasmonic nanoantennas can focus incident light into intense hotspots of the electromagnetic field, making them an essential building block for applications ranging from single molecule fluorescence enhancement to nanoscale photodetection [88–90]. The strong nearfields also enable the high sensitivity of such structures towards refractive index changes in, e.g., the nanoscale gap of a plasmonic dimer antenna [91, 92]. Extending this towards catalytic systems, Liu et al. utilized the concept of antenna-enhancement for hydrogen sensing by placing a small palladium disk in the nanofocus of a triangular gold nanoantenna [93]. Compared to previous experiments that studied, e.g., resonant plasmonic nanodisks with diameters in the 200–300 nm range, the authors were able to examine the hydrogen uptake and release trajectories of Pd particles down to 60 nm in size. The Pd/PdH transition in such small particles is very challenging to detect optically, since the high intrinsic damping of Pd causes the Pd nanoparticles to exhibit a very low optical response at visible wavelengths. The hybrid antenna/disk structures were fabricated using two-step electron-beam lithography, and precise alignment between the two exposure processes was achieved through the use of gold alignment marks. This allowed for

the reliable positioning of the Pd disk adjacent to the triangular Au antenna with inter-particle gaps down to 10 nm. The authors first exposed this optimized sample to controlled cycles of hydrogen gas while recording the optical scattering response from a single antenna/disk structure. They observed a pronounced plasmonic scattering peak at a wavelength of 638 nm, which underwent a spectral redshift of up to 9 nm for exposure to a hydrogen concentration of 16 Torr, equivalent to a concentration of 2 vol.%. When purging the system with nitrogen, a net redshift of 4 nm remained, demonstrating the presence of hysteresis in a single nanoscale Pd/PdH particle. In a subsequent second exposure cycle, the deterioration of the Pd/PdH particle associated with the hysteresis behavior led to somewhat lower redshifts (Fig. 8.10a). Also, an increase of the antenna-nanoparticle distance caused a severe drop of the sensing performance, again elucidating the important role of strong plasmonic field-enhancement.

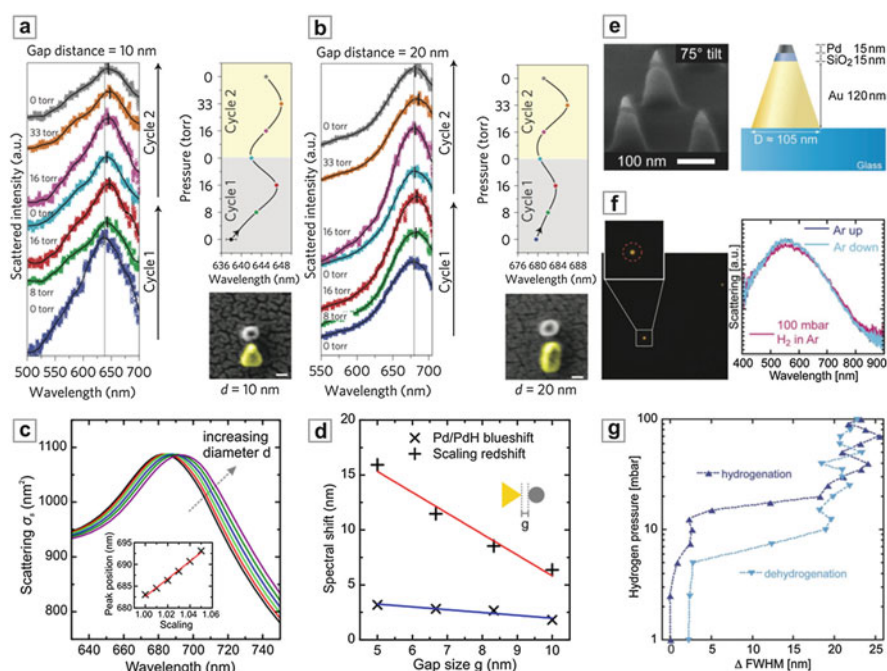


Fig. 8.10 Antenna-enhanced sensor geometries. (a) Optical scattering measurements and plasmon resonance shifts for a single palladium-gold triangle antenna during two hydrogen uptake and release cycles. (b) Hydrogen-dependent measurements for a single palladium-gold rod antenna (a, b from [93]). (c) Numerically calculated single particle scattering spectra for different diameters of the Pd disk next to the triangular Au antenna (initial gap size $g = 7$ nm). (d) Resonance shifts due to the Pd/PdH transition and the growing of the Pd disk for different initial gap sizes g (c, d from [94]). (e) SEM image and schematic depiction of a 120 nm high, truncated Au nanocone with a 15 nm SiO₂ spacer layer and a Pd particle on the tip. (f) Dark-field optical image of a single nanocone (left) and its spectral response to 100 vol.% Ar, 10 vol.% H₂ in Ar, and 100 vol.% Ar (right). (g) Corresponding optical isotherm of the nanocone system during hydrogenation (e–g from [97])

The crucial influence of antenna shape was demonstrated by replacing the triangular nanoantenna with a simple Au rod antenna. In this geometry, the authors found that the spectral shifts were roughly half smaller compared to those of the triangular system (Fig. 8.10b), showing that the sharp tip of the single bowtie antenna is essential to obtain an intense nanofocus and consequently high sensitivity.

The detailed reason for the experimentally observed spectral shifts was further investigated by Tittl et al. who performed numerical simulations on the discussed nanoantenna-enhanced sensor geometry [94]. They modeled the system using geometrical parameters extracted from the experimental SEM micrographs as well as optical constants for Au and Pd/PdH from literature, and calculated the scattering response of single antenna/disk sensor devices using a commercial finite element (FEM) electromagnetic field solver. This allowed them to investigate the two main features of the Pd/PdH transition, the dielectric change and the lattice expansion, independently from each other. The authors started with the hydrogen-induced dielectric change, since it constitutes the dominant effect for less complex Pd-based sensor geometries [95, 96]. However, when changing the dielectric function of the disk from Pd to PdH, the authors observed a small blueshift of 3 nm instead of the expected pronounced redshift of 9 nm from experiment. To model the effect of lattice expansion, both the diameter and the height of the Pd nanodisk were scaled with a factor s , ranging from 1.00 (no expansion) to 1.04 (maximum expansion from literature [56]). This led to a linear redshift of the plasmon resonance peak, with a maximum value of 13 nm for a scaling of 1.04 (Fig. 8.10c). By combining this scaling with the dielectric function of PdH, the authors were able to perfectly reproduce the experimental results, a hydrogen-induced redshift of the plasmon peak together with significant broadening of the lineshape. Additionally, the two competing spectral effects exhibited a markedly different scaling behavior: the blueshift associated with the dielectric change in the Pd remained mostly constant at 3 nm, whereas the redshift induced by the disk's scaling could be tuned via the gap size (Fig. 8.10d). In a comparison between triangular and rod antenna geometries, the authors also found the reduction of the sensing performance from experiment. However, when considering a double rod antenna geometry by adding a second antenna arm opposite the first, they observed a large redshift of 28 nm, comparable to a double bowtie geometry. This elucidates how the strong field-enhancement in the feed gap of a double antenna becomes dominant over the shape of the single antenna elements, allowing for high sensing performance with easier to fabricate constituent elements.

Still, the precise relative positioning of particles with different material properties and the required multi-layer processing pose significant challenges for high-throughput fabrication. To alleviate this, Langhammer et al. have utilized hole-mask colloidal lithography to fabricate truncated gold nanocones with functionalized tips to detect the hydrogen sorption and desorption kinetics of palladium and magnesium (Mg) nanoparticles [97]. Au nanocone antennas with different truncation height and consequently tip sharpness were fabricated and subsequently covered with a SiO₂ spacer layer and the reactive material in question. For a nanocone height of 120 nm, a 15 nm spacer layer, and a 15 nm thick tip, the authors were able

to obtain an antenna-enhanced system with an Pd particle only 30 nm in size (Fig. 8.10e), a factor of 2 smaller than in the experiment by Liu et al. [93]. Still, the authors were able to detect the optical scattering response from single nanocones and could observe clear and reversible shifts of the plasmon scattering peak when exchanging the gaseous environment from 100 vol.% Ar to 10 vol.% H₂ and back to Ar (Fig. 8.10f). To further study the phase-transition behavior in the Pd nanoparticle, complete isotherms hydrogenation and dehydrogenation were recorded at different temperatures. Especially, the authors chose to track the full width at half maximum (FWHM) of the plasmon peak vs. the hydrogen partial pressure instead of the more common spectral shift or peak intensity change, allowing them to observe a clear hysteresis behavior from a single 30 nm Pd particle coupled to a Au nanocone antenna (Fig. 8.10g). Using Van't Hoff analysis, they were able to extract the enthalpy and entropy of hydride formation from the isotherm measurements, indicating a destabilization of the PdH phase compared to the bulk material. Furthermore, the authors extended the nanocone concept to the study of the hydrogenation kinetics of a single Mg nanoparticle. To prevent alloying and isolate the Mg particle from neighboring materials, it was placed between two titanium (Ti) layers, with a thin catalytic Pd layer placed at the top of the structure. This system configuration allowed the authors to trace a full hydrogenation isotherm for a single Mg nanodisk with a diameter of only 35 nm, demonstrating the versatility of their detection scheme. By implementing such advanced, high-throughput fabrication methods, complex plasmonic sensing geometries can be transitioned from high-resolution single-particle spectroscopy towards large-area technological applications, allowing for the sensitive, robust, and cost-effective detection of a variety of reagents and chemical processes.

8.9 Conclusions and Outlook

Plasmonic gas and chemical sensing has evolved from simple functionalized thin films towards increasingly complex and highly sensitive nanodevices for detection of a plethora of chemical reagents. Especially, the development of hybrid plasmonic structures, which combine several materials to incorporate new functionalities and achieve selectivity, has enabled an unprecedented flexibility in the design of sensor nanodevices. Aided by straightforward optical and thus non-invasive readout, plasmonic sensor devices have thus demonstrated sensitivities down to the ppm range combined with extremely small sensing volumes and reproducible operation. Based on these past achievements, plasmonic nanosensors need to overcome two main challenges in the future. In basic science, the ultimate limit of plasmonic chemical detection is still under debate. To resolve this and to extend current approaches towards gas sensing at the single molecule level, a combination of highly stable spectroscopic techniques and novel nanodevices with pronounced reagent-induced optical responses will be highly desirable. In the context of industrial applications, the requirements of high-throughput, cost-effective fabrication and

especially long-term stability have to be met, ensuring that the devices can withstand a move from laboratory conditions to realistic and possibly harsh environments. With this, plasmonic nanosensor devices will serve as an essential building block both for nanomaterials science and advanced industrial process monitoring.

Acknowledgements We are grateful to N. Strohfeldt and F. Neubrech for key advice and discussions. A.T. and H.G. were financially supported by the Deutsche Forschungsgemeinschaft (SPP1391, FOR730, GI 269/11-1), the Bundesministerium für Bildung und Forschung (13 N9048 and 13 N10146), the ERC Advanced Grant COMPLEXPLAS, the Baden-Württemberg Stiftung (Spitzenforschung II), and the Ministerium für Wissenschaft, Forschung und Kunst Baden-Württemberg (Az: 7533-7-11.6-8). N.L. was supported by the Sofia Kovalevskaja Award of the Alexander von Humboldt Foundation and Grassroots Proposal M10331 from the Max Planck Institute for Intelligent Systems.

References

1. Valentine J, Zhang S, Zentgraf T, Ulin-Avila E, Genov DA, Bartal G, Zhang X (2008) Three-dimensional optical metamaterial with a negative refractive index. *Nature* 455:376–379
2. Atwater HA, Polman A (2010) Plasmonics for improved photovoltaic devices. *Nat Mater* 9:205–213
3. Boisselier E, Astruc D (2009) Gold nanoparticles in nanomedicine: preparations, imaging, diagnostics, therapies and toxicity. *Chem Soc Rev* 38:1759–1782
4. Kelly KL, Coronado E, Zhao LL, Schatz GC (2003) The optical properties of metal nanoparticles: the influence of size, shape, and dielectric environment. *J Phys Chem B* 107:668–677
5. Haynes CL, Van Duyne RP (2001) Nanosphere lithography: a versatile nanofabrication tool for studies of size-dependent nanoparticle optics. *J Phys Chem B* 105:5599–5611
6. Guo LJ (2007) Nanoimprint lithography: methods and material requirements. *Adv Mater* 19:495–513
7. Larsson EM, Syrenova S, Langhammer C (2012) Nanoplasmonic sensing for nanomaterials science. *Nanophotonics* 1:249–266
8. Mayer KM, Hafner JH (2011) Localized surface plasmon resonance sensors. *Chem Rev* 111:3828–3857
9. Anker JN, Hall WP, Lyandres O, Shah NC, Zhao J, Van Duyne RP (2008) Biosensing with plasmonic nanosensors. *Nat Mater* 7:442–453
10. Willets KA, Van Duyne RP (2007) Localized surface plasmon resonance spectroscopy and sensing. *Annu Rev Phys Chem* 58:1–33
11. Lal S, Link S, Halas NJ (2007) Nano-optics from sensing to wave guiding. *Nat Photonics* 1:641–648
12. Maier SA (2007) *Plasmonics: fundamentals and applications*. Springer, New York
13. Hartland GV (2011) Optical studies of dynamics in noble metal nanostructures. *Chem Rev* 111:3858–3887
14. Hu M, Novo C, Funston A, Wang H, Staleva H, Zou S, Mulvaney P, Xia Y, Hartland GV (2008) Dark-field microscopy studies of single metal nanoparticles: understanding the factors that influence the linewidth of the localized surface plasmon resonance. *J Mater Chem* 18:1949
15. Sönnichsen C, Franzl T, Wilk T, von Plessen G, Feldmann J (2002) Drastic reduction of plasmon damping in gold nanorods. *Phys Rev Lett* 88:077402
16. Halas NJ, Lal S, Chang W-S, Link S, Nordlander P (2011) Plasmons in strongly coupled metallic nanostructures. *Chem Rev* 111:3913–3961
17. Liu N, Langguth L, Weiss T, Kästel J, Fleischhauer M, Pfau T, Giessen H (2009) Plasmonic analogue of electromagnetically induced transparency at the Drude damping limit. *Nat Mater* 8:758–762

18. Tassin P, Zhang L, Zhao R, Jain A, Koschny T, Soukoulis C (2012) Electromagnetically induced transparency and absorption in metamaterials: the radiating two-oscillator model and its experimental confirmation. *Phys Rev Lett* 109:187401
19. Miroshnichenko A, Flach S, Kivshar Y (2010) Fano resonances in nanoscale structures. *Rev Mod Phys* 82:2257–2298
20. Novotny L, van Hulst N (2011) Antennas for light. *Nat Photonics* 5:83–90
21. Muhlischlegel P, Eisler H-J, Martin OJF, Hecht B, Pohl DW (2005) Resonant optical antennas. *Science* 308:1607–1609
22. Zuloaga J, Prodan E, Nordlander P (2010) Quantum plasmonics: optical properties and tunability of metallic nanorods. *ACS Nano* 4:5269–5276
23. Savage KJ, Hawkeye MM, Esteban R, Borisov AG, Aizpurua J, Baumberg JJ (2013) Revealing the quantum regime in tunnelling plasmonics. *Nature* 491:574–577
24. Scholl JA, García-Extarri A, Koh AL, Dionne JA (2013) Observation of quantum tunneling between two plasmonic nanoparticles. *Nano Lett* 13:564–569
25. Larsson EM, Langhammer C, Zoric I, Kasemo B (2009) Nanoplasmonic probes of catalytic reactions. *Science* 326:1091–1094
26. Korotcenkov G (2005) Gas response control through structural and chemical modification of metal oxide films: state of the art and approaches. *Sens Actuators B* 107:209–232
27. Eranna G, Joshi BC, Runthala DP, Gupta RP (2004) Oxide materials for development of integrated gas sensors – a comprehensive review. *Crit Rev Solid State Mater Sci* 29:111–188
28. Ando M, Kobayashi T, Iijima S, Haruta M (2003) Optical CO sensitivity of Au-CuO composite film by use of the plasmon absorption change. *Sens Actuators B* 96:589–595
29. Sirinakis G, Siddique R, Manning I, Rogers PH, Carpenter MA (2006) Development and characterization of Au–YSZ surface plasmon resonance based sensing materials: high temperature detection of CO. *J Phys Chem B* 110:13508–13511
30. Buttner WJ, Post MB, Burgess R, Rivkin C (2011) An overview of hydrogen safety sensors and requirements. *Int J Hydrog Energy* 36:2462–2470
31. Linic S, Christopher P, Ingram DB (2011) Plasmonic-metal nanostructures for efficient conversion of solar to chemical energy. *Nat Mater* 10:911–921
32. Buso D, Busato G, Guglielmi M, Martucci A, Bello V, Mattei G, Mazzoldi P, Post ML (2007) Selective optical detection of H₂ and CO with SiO₂ sol – gel films containing NiO and Au nanoparticles. *Nanotechnology* 18:475505
33. Dharmalingam G, Joy NA, Grisafe B, Carpenter MA (2012) Plasmonics-based detection of H₂ and CO: discrimination between reducing gases facilitated by material control. *Beilstein J Nanotechnol* 3:712–721
34. Rogers PH, Sirinakis G, Carpenter MA (2008) Direct observations of electrochemical reactions within Au-YSZ thin films via absorption shifts in the Au nanoparticle surface plasmon resonance. *J Phys Chem C* 112:6749–6757
35. Ohodnicki PR, Wang C, Natesakhawat S, Baltrus JP, Brown TD (2012) In-situ and ex-situ characterization of TiO₂ and Au nanoparticle incorporated TiO₂ thin films for optical gas sensing at extreme temperatures. *J Appl Phys* 111:064320
36. Della Gaspera E, Guglielmi M, Agnoli S, Granozzi G, Post ML, Bello V, Mattei G, Martucci A (2010) Au nanoparticles in nanocrystalline TiO₂– NiO films for SPR-based, selective H₂S gas sensing. *Chem Mater* 22:3407–3417
37. Rogers PH, Sirinakis G, Carpenter MA (2008) Plasmonic-based detection of NO₂ in a harsh environment. *J Phys Chem C* 112:8784–8790
38. Kneipp K, Kneipp H, Itzkan I, Dasari RR, Feld MS (1999) Ultrasensitive chemical analysis by Raman spectroscopy. *Chem Rev* 99:2957–2976
39. Kneipp K, Wang Y, Kneipp H, Perelman L, Itzkan I, Dasari R, Feld M (1997) Single molecule detection using surface-enhanced Raman scattering (SERS). *Phys Rev Lett* 78:1667–1670
40. Li JF, Huang YF, Ding Y, Yang ZL, Li SB, Zhou XS, Fan FR, Zhang W, Zhou ZY, De Wu Y, Ren B, Wang ZL, Tian ZQ (2010) Shell-isolated nanoparticle-enhanced Raman spectroscopy. *Nature* 464:392–395
41. Qian K, Liu H, Yang L, Liu J (2012) Functionalized shell-isolated nanoparticle-enhanced Raman spectroscopy for selective detection of trinitrotoluene. *Analyst* 137:4644–4646

42. Zhang BQ, Li SB, Xiao Q, Li J, Sun JJ (2013) Rapid synthesis and characterization of ultra-thin shell Au@ SiO₂ nanorods with tunable SPR for shell-isolated nanoparticle-enhanced Raman spectroscopy (SHINERS). *J Raman Spectrosc* 44:1120–1125
43. Fan X, White IM, Shopova SI, Zhu H, Suter JD, Sun Y (2008) Sensitive optical biosensors for unlabeled targets: a review. *Anal Chim Acta* 620:8–26
44. Bingham JM, Anker JN, Kreno LE, Van Duyne RP (2010) Gas sensing with high-resolution localized surface plasmon resonance spectroscopy. *J Am Chem Soc* 132:17358–17359
45. Dahlin AB, Tegenfeldt JO, Höök F (2006) Improving the instrumental resolution of sensors based on localized surface plasmon resonance. *Anal Chem* 78:4416–4423
46. Jans H, Huo Q (2012) Gold nanoparticle-enabled biological and chemical detection and analysis. *Chem Soc Rev* 41:2849
47. Yang J, Yang J, Ying JY (2012) Morphology and lateral strain control of Pt nanoparticles via core – shell construction using alloy AgPd core toward oxygen reduction reaction. *ACS Nano* 6:9373–9382
48. Christian ML, Aguey-Zinsou K-F (2012) Core-shell strategy leading to high reversible hydrogen storage capacity for NaBH₄. *ACS Nano* 6:7739–7751
49. Hsieh Y-C, Zhang Y, Su D, Volkov V, Si R, Wu L, Zhu Y, An W, Liu P, He P, Ye S, Adzic RR, Wang JX (2013) Ordered bilayer ruthenium – platinum core-shell nanoparticles as carbon monoxide-tolerant fuel cell catalysts. *Nat Commun* 4:2466
50. Ghodselahi T, Zahrahi H, Saani MH, Vesaghi MA (2011) CO gas sensor properties of Cu@CuO core – shell nanoparticles based on localized surface plasmon resonance. *J Phys Chem C* 115:22126–22130
51. Vasileva P, Donkova B, Karadjova I, Dushkin C (2011) Synthesis of starch-stabilized silver nanoparticles and their application as a surface plasmon resonance-based sensor of hydrogen peroxide. *Colloids Surf A Physicochem Eng Asp* 382:203–210
52. Halliwell B, Clement MV, Long LH (2000) Hydrogen peroxide in the human body. *FEBS Lett* 486:10–13
53. Endo T, Shibata A, Yanagida Y, Higo Y, Hatsuzawa T (2010) Localized surface plasmon resonance optical characteristics for hydrogen peroxide using polyvinylpyrrolidone coated silver nanoparticles. *Mater Lett* 64:2105–2108
54. Hill RT, Mock JJ, Hucknall A, Wolter SD, Jokerst NM, Smith DR, Chilkoti A (2012) Plasmon ruler with angstrom length resolution. *ACS Nano* 6:9237–9246
55. Ciraci C, Hill RT, Mock JJ, Urzhumov Y, Fernández-Domínguez AI, Maier SA, Pendry JB, Chilkoti A, Smith DR (2012) Probing the ultimate limits of plasmonic enhancement. *Science* 337:1072–1074
56. Flanagan TB, Oates WA (1991) The palladium-hydrogen system. *Annu Rev Mater Sci* 21:269–304
57. Jewell L, Davis B (2006) Review of absorption and adsorption in the hydrogen-palladium system. *Appl Catal Gen* 310:1–15
58. Yamauchi M, Ikeda R, Kitagawa H, Takata M (2008) Nanosize effects on hydrogen storage in palladium. *J Phys Chem C* 112:3294–3299
59. Khanuja M, Mehta BR, Agar P, Kulriya PK, Avasthi DK (2009) Hydrogen induced lattice expansion and crystallinity degradation in palladium nanoparticles: effect of hydrogen concentration, pressure, and temperature. *J Appl Phys* 106:093515
60. Tang ML, Liu N, Dionne JA, Alivisatos AP (2011) Observations of shape-dependent hydrogen uptake trajectories from single nanocrystals. *J Am Chem Soc* 133:13220–13223
61. Seo D, Park G, Song H (2012) Plasmonic monitoring of catalytic hydrogen generation by a single nanoparticle probe. *J Am Chem Soc* 134:1221–1227
62. Tittl A, Yin X, Giessen H, Tian X-D, Tian ZQ, Kremers C, Chigrin DN, Liu N (2013) Plasmonic smart dust for probing local chemical reactions. *Nano Lett* 13:1816–1821
63. Wang C, Ma L, Hossain M, Wang H, Zou S, Hickman JJ, Su M (2010) Direct visualization of molecular scale chemical adsorptions on solids using plasmonic nanoparticle arrays. *Sens Actuators B* 150:667–672

64. Morris T, Szulczewski G (2002) A spectroscopic ellipsometry, surface plasmon resonance, and X-ray photoelectron spectroscopy study of Hg adsorption on gold surfaces. *Langmuir* 18:2260–2264
65. Ahmadnia-Feyzabad S, Khodadadi AA, Vesali-Naseh M, Mortazavi Y (2012) Highly sensitive and selective sensors to volatile organic compounds using MWCNTs/SnO₂. *Sens Actuators B* 166–167:150–155
66. Silva LIB, Freitas AC, Rocha-Santos TAP, Pereira ME, Duarte AC (2011) Breath analysis by optical fiber sensor for the determination of exhaled organic compounds with a view to diagnostics. *Talanta* 83:1586–1594
67. Ma W, Luo J, Ling W, Wang W (2013) Chloroform-sensing properties of plasmonic nanostructures using poly(methyl methacrylate) transduction layer. *Micro Nano Lett* 8:111–114
68. Langhammer C, Zorić I, Kasemo B, Clemens BM (2007) Hydrogen storage in Pd nanodisks characterized with a novel nanoplasmonic sensing scheme. *Nano Lett* 7:3122–3127
69. Strohfeldt N, Tittl A, Giessen H (2013) Long-term stability of capped and buffered palladium-nickel thin films and nanostructures for plasmonic hydrogen sensing applications. *Opt Mater Express* 3:194–204
70. Prodan E (2003) A hybridization model for the plasmon response of complex nanostructures. *Science* 302:419–422
71. Hentschel M, Dregely D, Vogelgesang R, Giessen H, Liu N (2011) Plasmonic oligomers: the role of individual particles in collective behavior. *ACS Nano* 5:2042–2050
72. Rahmani M, Lei DY, Giannini V, Lukiyanchuk B, Ranjbar M, Liew TYF, Hong M, Maier SA (2012) Subgroup decomposition of plasmonic resonances in hybrid oligomers: modeling the resonance lineshape. *Nano Lett* 12:2101–2106
73. Schider G, Krenn JR, Gotschy W, Lamprecht B, Ditlbacher H, Leitner A, Aussenegg FR (2001) Optical properties of Ag and Au nanowire gratings. *J Appl Phys* 90:3825
74. Tikhodeev SG, Yablonskii AL, Muljarov EA, Gippius NA, Ishihara T (2002) Quasiguidded modes and optical properties of photonic crystal slabs. *Phys Rev B* 66:045102
75. Fan S, Joannopoulos J (2002) Analysis of guided resonances in photonic crystal slabs. *Phys Rev B* 65:235112
76. Christ A, Tikhodeev S, Gippius N, Kuhl J, Giessen H (2003) Waveguide-plasmon polaritons: strong coupling of photonic and electronic resonances in a metallic photonic crystal slab. *Phys Rev Lett* 91:183901
77. Nau D, SEidel A, Orzekowsky RB, Lee SH, Deb S, Giessen H (2010) Hydrogen sensor based on metallic photonic crystal slabs. *Opt Lett* 35:3150–3152
78. Valsecchi C, Brolo AG (2013) Periodic metallic nanostructures as plasmonic chemical sensors. *Langmuir* 29:5638–5649
79. Brolo AG, Gordon R, Leathem B, Kavanagh KL (2004) Surface plasmon sensor based on the enhanced light transmission through arrays of nanoholes in gold films. *Langmuir* 20:4813–4815
80. Ebbesen TW, Lezec HJ, Ghaemi HF, Thio T, Wolff PA (1998) Extraordinary optical transmission through sub-wavelength hole arrays. *Nature* 391:667–669
81. Maeda E, Mikuriya S, Endo K, Yamada I, Suda A, Delaunay J-J (2009) Optical hydrogen detection with periodic subwavelength palladium hole arrays. *Appl Phys Lett* 95:133504
82. Moreau A, Ciraci C, Mock JJ, Hill RT, Wang Q, Wiley BJ, Chilkoti A, Smith DR (2013) Controlled-reflectance surfaces with film-coupled colloidal nanoantennas. *Nature* 492:86–89
83. Chen K, Adato R, Altug H (2012) Dual-band perfect absorber for multispectral plasmon-enhanced infrared spectroscopy. *ACS Nano* 6:7998–8006
84. Liu N, Mesch M, Weiss T, Hentschel M, Giessen H (2010) Infrared perfect absorber and its application as plasmonic sensor. *Nano Lett* 10:2342–2348
85. Landy N, Sajuyigbe S, Mock J, Smith DR, Padilla WJ (2008) Perfect metamaterial absorber. *Phys Rev Lett* 100:207402
86. Tittl A, Mai P, Taubert R, Dregely D, Liu N, Giessen H (2011) Palladium-based plasmonic perfect absorber in the visible wavelength range and its application to hydrogen sensing. *Nano Lett* 11:4366–4369

87. Fedtke P, Wienecke M, Bunescu M-C, Pietrzak M, Deistung K, Borchardt E (2004) Hydrogen sensor based on optical and electrical switching. *Sens Actuators B* 100:151–157
88. Kinkhabwala A, Yu Z, Fan S, Avlasevich Y, Müllen K, Moerner WE (2009) Large single-molecule fluorescence enhancements produced by a bowtie nanoantenna. *Nat Photonics* 3:654–657
89. Duan H, Fernández-Domínguez AI, Bosman M, Maier SA, Yang JKW (2012) Nanoplasmonics: classical down to the nanometer scale. *Nano Lett* 12:1683–1689
90. Knight MW, Sobhani H, Nordlander P, Halas NJ (2011) Photodetection with active optical antennas. *Science* 332:702–704
91. Zhao Y, Engheta N, Alù A (2011) Effects of shape and loading of optical nanoantennas on their sensitivity and radiation properties. *J Opt Soc Am B* 28:1266
92. Liu N, Wen F, Zhao Y, Wang Y, Nordlander P, Halas NJ, Alù A (2012) Individual nanoantennas loaded by three-dimensional optical nanocircuits. *Nano Lett* 13(1):142–147
93. Liu N, Tang ML, Hentschel M, Giessen H, Alivisatos AP (2011) Nanoantenna-enhanced gas sensing in a single tailored nanofocus. *Nat Mater* 10:631–636
94. Tittl A, Kremers C, Dorfmueller J, Chigrin DN, Giessen H (2012) Spectral shifts in optical nanoantenna-enhanced hydrogen sensors. *Opt Mater Express* 2:111–118
95. Wadell C, Antosiewicz TJ, Langhammer C (2012) Optical absorption engineering in stacked plasmonic Au-SiO(2)-Pd nanoantennas. *Nano Lett* 12:4784–4790
96. Dasgupta A, Kumar GVP (2012) Palladium bridged gold nanocylinder dimer: plasmonic properties and hydrogen sensitivity. *Appl Opt* 51:1688–1693
97. Shegai T, Langhammer C (2011) Hydride formation in single palladium and magnesium nanoparticles studied by nanoplasmonic dark-field scattering spectroscopy. *Adv Mater* 23:4409–4414